Research on Engineering Structures & Materials
www.jresm.org
Research Group

*Research Article*

# Integration of global navigation satellite systems (GNSS) and geographic information systems (GIS) for bridge structural deformation monitoring

B. Y. M. Younus [1,a], S. J. S. Hakim [*,1,b], S. Shahidan [1,c], S. S. M. Zuki [1,d], A. A. Sanaa [2,e]

[1]*Faculty of Civil Engineering and Built Environment, University Tun Hussein Onn Malaysia, 86400 Parit Raja, Batu Pahat, Johor, Malaysia*
[2]*The Higher Institute for Technology in Elmarj, Libya*

**Article Info**

***Article History:***

Received 06 July 2025

Accepted 18 Jan 2026

***Keywords:***

Structural deformation monitoring;
Global navigation satellite system;
Geographic information system;
Real-time kinematic;
Inverse distance weighting

**Abstract**

Monitoring structural deformation is essential for ensuring the safety and longevity of infrastructure. Traditional methods often face limitations in accuracy, efficiency, and spatial assessment. This study aims to combine Global Navigation Satellite Systems (GNSS) and Geographic Information Systems (GIS) to enhance monitoring capabilities by providing highly precise deformation data and enabling real-time analysis for the Fourth Bridge in Al-Marj, Libya. Displacement trajectories along the East, North, and Vertical axes were analyzed using Real-Time Kinematic (RTK) GNSS measurements collected during multiple observation sessions and interpolated with Inverse Distance Weighting (IDW) within ArcGIS. The findings reveal notable spatial and temporal displacements, with IDW-generated maps delineating high-risk zones of structural movement. Red zones signify substantial vertical deformation and potential instability, whereas green zones represent stable areas with minimal movement. Key results highlight localized displacements that warrant further investigation, while other regions remain stable. This research demonstrates the advantages of integrating GNSS and GIS for continuous structural monitoring, offering valuable insights into structural health and facilitating proactive maintenance strategies to enhance bridge safety. By employing GNSS for precise position tracking and GIS for effective spatial data management, this approach advances the detection and analysis of deformations, thereby supporting more informed decision-making in infrastructure maintenance and risk mitigation.



## 1. Introduction

Ensuring the reliability of in-service bridges requires ongoing monitoring of three-dimensional deformations, as unnoticed movements could increase safety risks and raise lifecycle costs [1]. Over the past decade, integrating the Global Navigation Satellite System (GNSS) with geographic information systems (GIS) has become an important part of structural health monitoring (SHM). GNSS offers accurate, high-frequency three-dimensional data at specific points, while GIS combines these measurements into verifiable, map-based evidence that supports asset-level decision-making [2]. In practical use, multi-GNSS processing on operational bridges has shown the ability to detect millimeter-level displacements in both dynamic and quasi-static responses of long-span and railway bridges [3,4]. For short baselines, real-time kinematic (RTK) solutions provide quick time-to-fix and positional accuracy at the centimeter-to-millimeter level, even over short observation periods, making them suitable for multi-epoch deformation monitoring campaigns [5,6].

*Corresponding author: seyedhakim@uthm.edu.my
[a]orcid.org/0009-0002-8116-6450; [b]orcid.org/0000-0002-4866-3116; [c]orcid.org/0000-0002-6034-9584; [d]orcid.org/0000-0001-8524-7456; [e]orcid.org/0000-0001-6406-9494
DOI: http://dx.doi.org/10.17515/resm2026-1009st0706rs

Independent research in bridge SHM confirms these results and highlights multi-constellation GNSS processing as a key enabler for achieving these capabilities [7,8].

Conversely, precise point positioning with ambiguity resolution (PPP/PPP-AR) eliminates the necessity for a local base station; however, it typically necessitates a convergence period prior to the availability of reliable displacement estimates. Recent advancements, particularly in ambiguity resolution and the Galileo High Accuracy Service (HAS), have reduced convergence times and improved vertical accuracy for monitoring applications [9], [10]. Network-assisted PPP (PPP-RTK) further diminishes convergence time through the application of external atmospheric and bias corrections, attaining sub-10-minute convergence for deformation monitoring and, under optimal conditions, nearly instantaneous solutions [11,12]. Independent assessments corroborate HAS's enhancements in vertical accuracy within operational settings [13], while market analyses anticipate broader adoption of HAS-enabled infrastructure monitoring [14]. Additionally, case studies demonstrate tangible operational and maintenance (O&M) benefits when analytical tools are integrated into GIS-based digital twins [15]. More broadly, recent architectural developments in bridge "digital twins" are transitioning GIS from static visualization toward integrated analytics, linking spatial databases with monitoring streams and analytical modules that facilitate maintenance planning and O&M workflows [16].

Despite recent advancements, three significant practical deficiencies persist. Firstly, numerous deployments are either site-specific or of short duration, thereby constraining the capacity to monitor component-level trends over time [17]. Secondly, the results are often presented as isolated time series lacking a consistent local reference frame, which impedes the comparison of ΔE, ΔN, and ΔU at fixed points across different campaigns [18]. Thirdly, GNSS–GIS integrations frequently end at visualization rather than progressing toward analytical coupling that correlates displacement vectors with inventory and condition data, thereby limiting the development of reproducible and auditable indicators for prioritization within resource constraints [19]. Contemporary reviews also underscore the importance of standardized local-frame implementations and rigorous, reproducible data governance in Structural Health Monitoring (SHM) [20].

A reproducible workflow has been established that (i) creates a stable local reference frame for consistent cross-campaign comparisons and (ii) integrates spatial analytics so that displacement fields inform decision-making rather than merely serving as figure-centric summaries. In this study, a consistent, multi-epoch workflow has been implemented, in which RTK positioning is performed and a fixed local ENU reference frame is defined. In addition, explicit quality control measures are applied to ensure that the resulting component-level displacement vectors (ΔE, ΔN, ΔU) are directly comparable across different campaigns. A structured GIS geodatabase subsequently links these vectors to bridge inventory and geostatistical surfaces, thereby providing condition-relevant indicators and robust prioritization evidence over multiple observation periods. The final outcome is a data-to-decision workflow that emphasizes trend detection and auditable indicators rather than single-snapshot visualization, thereby aligning GNSS accuracy with GIS-based analytics to support maintenance decisions within operational constraints [21,22].

## 2. Materials and Methods

### 2.1. Study Area

The study site is the Fourth Bridge in Al-Marj, Libya (approximately 32.5000° N, 20.7500° E), a vital urban crossing on the coastal plain road network. The surrounding corridor includes municipal roads and landscaped parcels that offer clear access for instruments and satellite visibility. As shown in Fig. 1, the deck supports bidirectional traffic and features a curved horizontal alignment. This alignment serves as the longitudinal axis of the local East–North–Up (ENU) frame in GNSS analysis.

The Fourth Bridge is a reinforced concrete, multi-span highway structure constructed in 1970; the most recent maintenance was conducted in 2010. The superstructure comprises a cast-in-place reinforced concrete (RC) deck slab supported by longitudinal precast, prestressed concrete (PSC)

girders, with diaphragms and cross-beams at interior supports. Expansion joints segment the deck, and its edges are protected by steel W-beam guardrails anchored to the deck edge. The substructure consists of reinforced concrete (RC) abutments with drainage weep holes and interior circular columns with tapered pier caps; solid hammerhead bents are incorporated. Elastomeric bearings are installed at both pier caps and abutments. Plan measurements indicate eight spans of 12.7 meters (total approximately 100 meters) and an unobstructed deck width of 8 meters. This fixed geometric layout, including the curved alignment, joint locations, and span sequence, functions as the structural reference for all subsequent GNSS-based assessments.

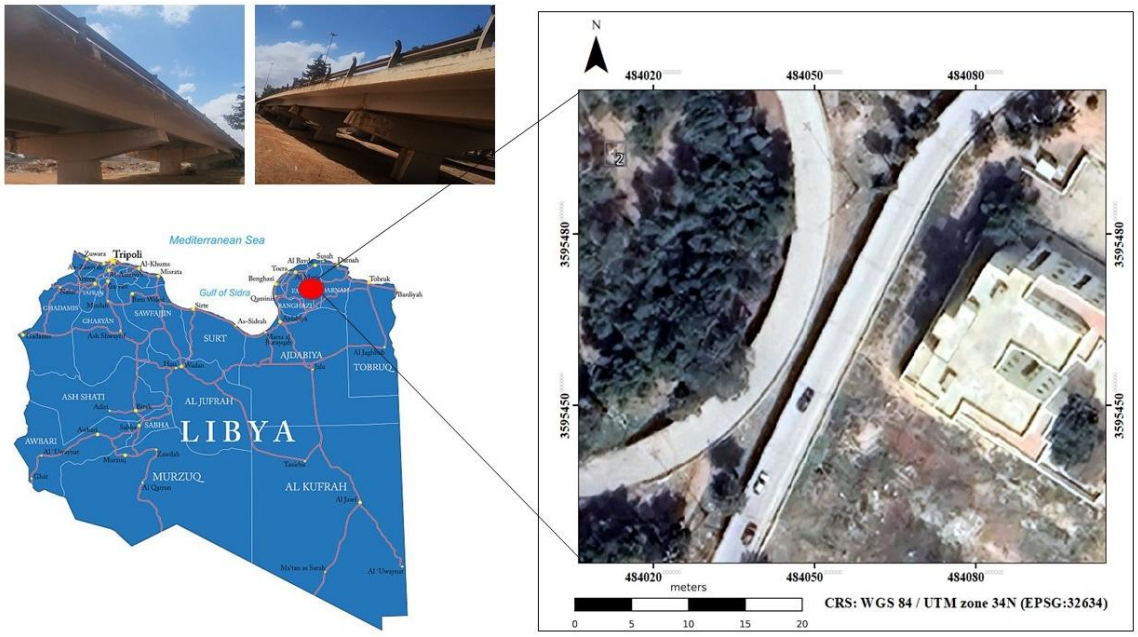


Fig. 1. Location of the Fourth Bridge in Al-Marj, Libya

## 2.2. Monitoring Scope and Rationale

This study examines the quasi-static displacement of decks and their spatial gradients under controlled conditions with the goal of facilitating screening-level priority mapping for inspections. By design, this methodology differs from dynamic response and load-rating analyses, which are typically conducted through controlled truck-load tests (diagnostic/proof), utilizing different instrumentation, safety protocols, and permitting procedures. Recent scholarly literature underscores that load testing constitutes a distinct methodological approach from routine quasi-static deformation mapping [23]. The focus aligns with current bridge Structural Health Monitoring (SHM) syntheses, which explicitly differentiate quasi-static deformation monitoring from dynamic and load-rating studies, and advocate for the customization of sensing and data collection in accordance with the target frequency content and decision-making objectives [24].

## 2.3. Thermal and Vibration Mitigation

Observation windows were conducted during traffic closures and under calm, dry conditions, outside strong thermal transients. The ambient temperatures for the four periods were approximately 24 °C (May), 30 °C (July), 27 °C (September), and 25 °C (November), as summarized in Table 1. These values are used operationally to qualify the interpretation of inter-epoch temperature differences (ΔT), as shown in Table 1, and suggest the likely environmental contribution to observed shifts (e.g., expansion from May to July, relaxation afterward), [25]. To reduce ambient vibrations, only fixed-ambiguity RTK epochs (1 Hz) were accepted, and per-station session means were calculated. Detectability is modeled below using a standard error approach. Peak-hour acquisitions were avoided to prevent non-stationary vehicle–bridge interactions, which can increase short-term variability.

Table 1. Thermal quality control by epoch and inter-epoch ΔT

| Epoch | Conditions | Ambient Temp (°C) | ΔT vs previous (°C) | Interpretation note |
|---|---|---|---|---|
| May | Calm, dry | 24 | — | Baseline (cool) |
| July | Calm, dry | 30 | +6 | The thermal expansion component likely |
| September | Calm, dry | 27 | −3 | Partial relaxation from July |
| November | Calm, dry | 25 | −2 | Near-baseline |

## 2.4. Acquisition Protocol and GIS-Based Interpolation Methods

This section represents the instrumentation and processing workflow. High-precision data were acquired utilizing Real-Time Kinematic (RTK) Global Navigation Satellite Systems (GNSS). Spatial interpolation and map generation were conducted within ArcMap 10.8. The workflow is designed to assess bridge integrity and generate actionable inputs for infrastructure management. The comprehensive research framework is depicted in Fig. 2.

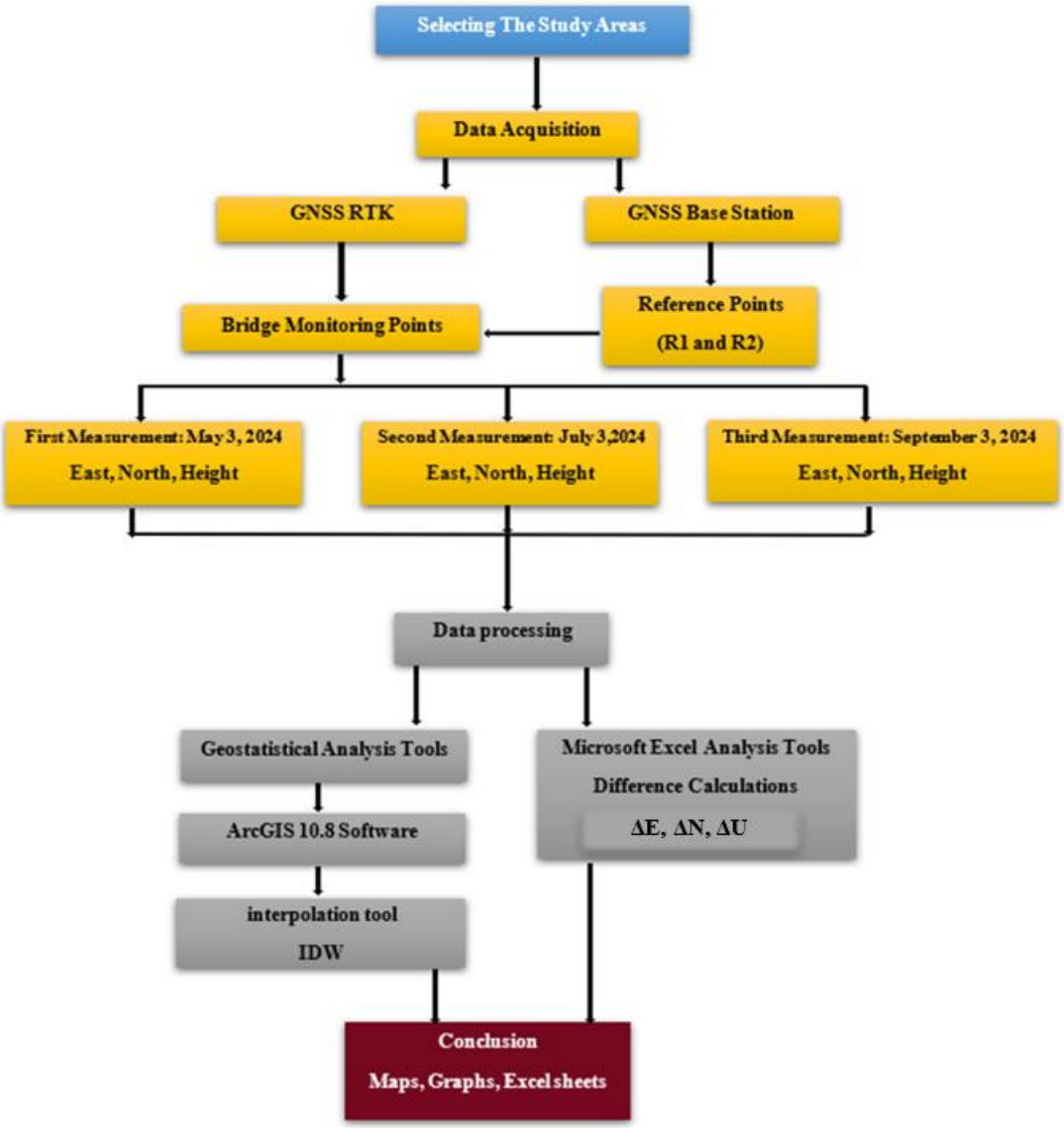


Fig. 2. Research framework of this study

### 2.4.1 Data Acquisition

A six-month, four-epoch monitoring program was conducted at two-month intervals (May 3, July 3, September 3, and November 4, 2024) to observe 18 GNSS stations arranged symmetrically across the bridge (nine on each side), capturing both longitudinal and transverse responses. Each campaign employed a short-baseline base–rover RTK setup with roughly 15-minute occupations per station. In collaboration with authorities, deck traffic was halted during all measurement periods to reduce load-induced dynamics and focus on quasi-static behavior. Observation windows were scheduled under calm, dry conditions with ambient temperatures around 24 °C (May), 30 °C (July), 27 °C (September), and 25 °C (November), minimizing meteorological effects and enabling direct comparisons across epochs.

Short-baseline RTK was selected to achieve repeatable, millimeter-level relative positions quickly. For baselines of a few tens of meters, RTK resolves integer ambiguities within seconds and offers stable centimeter- to millimeter-level accuracy, avoiding the convergence delays often encountered with PPP/PPP-RTK [26-27]. During campaign operations with station occupations of roughly 15 minutes, this rapid time-to-fix is essential [28]. Recent evaluations of PPP/PPP-RTK still reveal considerable convergence delays before achieving high-precision solutions, which supports the choice of RTK for this study's objectives [29]. Simultaneously, probabilistic SHM frameworks have been demonstrated to convert GNSS-derived dynamic displacements into reliability metrics and failure probabilities, helping to bridge the gap between displacement time series and risk-informed decision-making [30].

Table 2. Reference points (R1 and R2) for 3D control at the Fourth Bridge, Al-Marj, Libya

| Point | East (m) | North (m) | Height (m) | Description | Status |
|---|---|---|---|---|---|
| R 1 | 484117.855 | 3595509.56 | 365.887 | reference points | FIXED |
| R 2 | 483989.31 | 3595659.331 | 362.11 | reference points | FIXED |

Two permanent ground-control marks (R1, R2) provided by the Survey Department of Libya were validated before each RTK campaign through the use of dual-frequency static GNSS sessions lasting a minimum of 40 minutes. Subsequently, a minimally constrained least-squares network adjustment was conducted, with R1 fixed to establish the local datum and R2 treated as an independent check. This methodology verified the temporal stability of the control points. It also propagated accurate covariance information for subsequent RTK processing, in accordance with current standards for geodetic GNSS control based on static observations and rigorous least-squares adjustment [31]. The locations and coordinates of R1 and R2 for the four epochs are summarized in Table 2 and illustrated in Fig. 3.

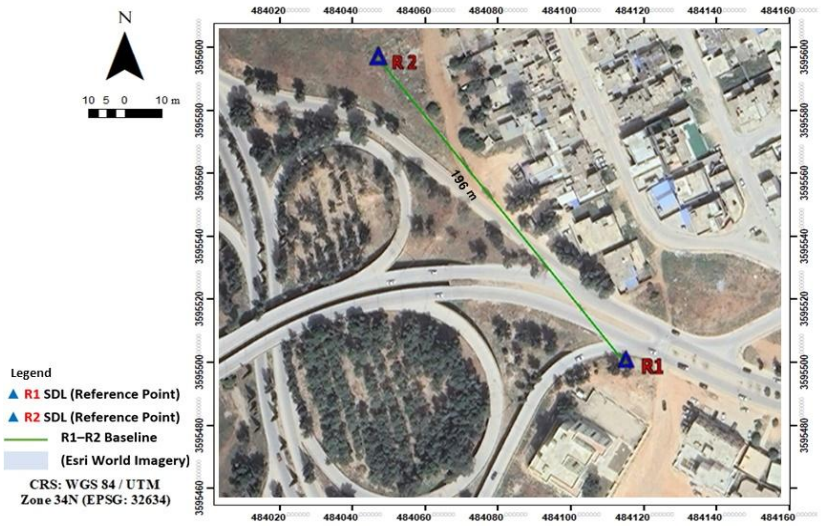


Fig. 3. Location of the 3-D control points

Data acquisition employed multi-frequency, multi-constellation STONEX S10 receivers in a short-baseline base–rover configuration for structural monitoring, as illustrated in Fig. 4. The S10 model facilitates carrier-phase RTK, thus enabling rapid and dependable resolution of integer ambiguities, and records both code and phase observations. This ensures stable performance even with minimal dwell times, utilizing the fixed-solution method [32]. All raw observational data, in conjunction with receiver metadata such as antenna model, measured antenna height, firmware version, and settings, were meticulously documented to guarantee complete traceability. Field operations were carried out under constraints related to deck traffic and environmental conditions, such as calm and dry weather, which provided optimal conditions for controlled data collection and resulted in millimeter-level repeatability across four observation periods.


Fig. 4. STONEX S10 GNSS

### *2.4.2 GNSS Processing Workflow (RTK): Rationale and Procedure*

A short-baseline real-time kinematic (RTK) method, fixed to a local baseline, was carried out during four survey campaigns on May 3, July 3, September 3, and November 4, 2024. RTK was chosen for its ability to use planar baselines from R1 to eighteen stations (about 23 to 108 meters), enabling quick integer ambiguity resolution and high relative accuracy within roughly fifteen-minute occupation periods. The in-situ datum at R1 allows immediate quality checks without external adjustments. Additionally, the study aims to evaluate relative structural deformation with millimeter-level repeatability. Before each survey, control verification between R1 and R2 was performed using dual-frequency static GNSS sessions of at least forty minutes, followed by a minimally constrained least-squares adjustment. This adjustment sets R1 as the reference and R2 as an independent check, confirming the local control stability over time. During each campaign, the base receiver was placed at R1 (coordinates: E = 484,117.855 m, N = 3,595,509.56 m, H = 365.887 m), while the rover was located at eighteen monitoring stations spread across the deck, piers, beams, and joints, as shown in Fig. 5. Field data collection used fixed-ambiguity solutions, a fifteen-degree elevation mask, and continuous visibility monitoring. Data epochs with PDOP values over four, signal loss, or cycle slips were excluded. Fixed solutions at one Hertz were averaged for each station after quality checks to reduce transient traffic effects and focus on quasi-static behavior during routine operations, excluding controlled load testing.

All numerical processing was conducted utilizing the Stonex Cube-Manager software. The workflow encompassed: (i) importing S10 observations alongside antenna metadata; (ii) implementing quality controls such as a 15° elevation mask, PDOP ≤ 4, removal of non-fixed epochs, and cycle slips; (iii) establishing the local control through an R1/R2 static adjustment, with R1 fixed as the datum and R2 serving as an independent check; and (iv) computing per-station campaign solutions by averaging 1 Hz fixed epochs post-QC. Solutions for all four campaigns were stored in WGS 84 / UTM zone 34N (EPSG:32634), including ellipsoidal heights. Coordinate files were output to three decimal places (0.001 m) for format consistency and traceability, without implying absolute accuracy. Displacements and comparisons are reported using significant figures and uncertainty bounds derived from the study's uncertainty model, which governs detectability and

confidence levels. The positional solutions for all 18 monitoring stations (PN1–PN18) across the four campaigns are summarized in Table 3, including UTM Easting, Northing, and ellipsoidal height values.

Table 3. RTK-GNSS observations across four epochs (UTM 34N)

| | First Measurement | | | Second measurement | | |
|---|---|---|---|---|---|---|
| PN | East (m) | North(m) | Height(m) | East(m) | North(m) | Height(m) |
| 1 | 484094.862 | 3595509.216 | 367.412 | 484094.854 | 3595509.211 | 367.403 |
| 2 | 484090.624 | 3595513.614 | 366.889 | 484090.618 | 3595513.61 | 366.878 |
| 3 | 484082.844 | 3595508.497 | 367.071 | 484082.841 | 3595508.493 | 367.066 |
| 4 | 484086.348 | 3595504.162 | 366.772 | 484086.339 | 3595504.153 | 366.761 |
| 5 | 484077.656 | 3595495.676 | 366.917 | 484077.647 | 3595495.669 | 366.911 |
| 6 | 484073.491 | 3595499.013 | 367.154 | 484073.479 | 3595499.004 | 367.146 |
| 7 | 484067.179 | 3595489.05 | 367.386 | 484067.179 | 3595489.05 | 367.386 |
| 8 | 484072.021 | 3595486.53 | 367.048 | 484072.014 | 3595486.525 | 367.041 |
| 9 | 484065.563 | 3595474.593 | 367.096 | 484065.559 | 3595474.591 | 367.093 |
| 10 | 484061.032 | 3595477.399 | 367.359 | 484061.03 | 3595477.399 | 367.358 |
| 11 | 484055.609 | 3595467.162 | 367.297 | 484055.609 | 3595467.162 | 367.297 |
| 12 | 484060.44 | 3595464.735 | 367.081 | 484060.44 | 3595464.735 | 367.081 |
| 13 | 484054.008 | 3595452.543 | 366.871 | 484054.008 | 3595452.543 | 366.871 |
| 14 | 484049.253 | 3595455.062 | 367.008 | 484049.253 | 3595455.062 | 367.008 |
| 15 | 484044.192 | 3595445.138 | 366.651 | 484044.187 | 3595445.132 | 366.643 |
| 16 | 484048.524 | 3595442.172 | 366.547 | 484048.517 | 3595442.164 | 366.536 |
| 17 | 484042.784 | 3595431.849 | 366.025 | 484042.775 | 3595431.837 | 366.015 |
| 18 | 484038.482 | 3595434.199 | 366.151 | 484038.478 | 3595434.192 | 366.145 |
| | Third Measurement | | | Fourth measurement | | |
| PN | East(m) | North(m) | Height(m) | East(m) | North(m) | Height(m) |
| 1 | 484094.843 | 3595509.202 | 367.396 | 484094.835 | 3595509.194 | 367.387 |
| 2 | 484090.614 | 3595513.606 | 366.872 | 484090.61 | 3595513.601 | 366.868 |
| 3 | 484082.838 | 3595508.488 | 367.06 | 484082.833 | 3595508.484 | 367.056 |
| 4 | 484086.331 | 3595504.146 | 366.753 | 484086.323 | 3595504.138 | 366.744 |
| 5 | 484077.64 | 3595495.662 | 366.903 | 484077.632 | 3595495.654 | 366.896 |
| 6 | 484073.475 | 3595499 | 367.143 | 484073.472 | 3595499 | 367.139 |
| 7 | 484067.176 | 3595489.047 | 367.384 | 484067.172 | 3595489.045 | 367.38 |
| 8 | 484072.005 | 3595486.519 | 367.033 | 484071.998 | 3595486.512 | 367.025 |
| 9 | 484065.554 | 3595474.587 | 367.087 | 484065.551 | 3595474.583 | 367.082 |
| 10 | 484061.026 | 3595477.396 | 367.353 | 484061.022 | 3595477.392 | 367.351 |
| 11 | 484055.609 | 3595467.162 | 367.294 | 484055.606 | 3595467.16 | 367.291 |
| 12 | 484060.438 | 3595464.732 | 367.076 | 484060.433 | 3595464.728 | 367.07 |
| 13 | 484054.003 | 3595452.538 | 366.864 | 484053.997 | 3595452.532 | 366.858 |
| 14 | 484049.25 | 3595455.06 | 367.003 | 484049.249 | 3595455.06 | 367.001 |
| 15 | 484044.182 | 3595445.127 | 366.637 | 484044.18 | 3595445.122 | 366.633 |
| 16 | 484048.51 | 3595442.157 | 366.528 | 484048.501 | 3595442.148 | 366.52 |
| 17 | 484042.767 | 3595431.828 | 366.006 | 484042.76 | 3595431.82 | 365.996 |
| 18 | 484038.474 | 3595434.186 | 366.139 | 484038.47 | 3595434.18 | 366.134 |

To identify the fundamental components, local East–North–Up (ENU) coordinates are computed within a reference frame at point R1. The geodetic coordinates of R1 on WGS-84, denoted as ($\varphi_0$, $\lambda_0$, $h_0$), are transformed into Earth-Centered, Earth-Fixed (ECEF) coordinates ($X_0$, $Y_0$, $Z_0$). For each rover epoch, station ECEF coordinates (X, Y, Z) are obtained from the RTK solution. The ECEF difference vector, $\Delta r = [X - X_0, Y - Y_0, Z - Z_0]^T$, is rotated into the local ENU frame utilizing the standard WGS-84 ECEF→ENU rotation matrix at ($\varphi_0$, $\lambda_0$). Employing R1 as the ENU origin prevents projection artifacts and ensures that the axes are aligned with the bridge's orientation.

Table 4. Local ENU solutions for the four measurement periods

| | First Measurement | | | Second measurement | | |
|---|---|---|---|---|---|---|
| PN | E(m) | **N**(m) | U(m) | E(m) | N(m) | U(m) |
| 1 | 23.003 | 0.381 | 1.525 | 23.011 | 0.386 | 1.516 |
| 2 | 27.250 | 4.013 | 1.002 | 27.256 | 4.009 | 0.991 |
| 3 | 35.025 | 1.119 | 1.184 | 35.028 | 1.123 | 1.179 |
| 4 | 31.513 | 5.450 | 0.885 | 31.522 | 5.459 | 0.874 |
| 5 | 40.195 | 13.954 | 1.030 | 40.204 | 13.961 | 1.024 |
| 6 | 44.367 | 10.622 | 1.267 | 44.379 | 10.631 | 1.259 |
| 7 | 50.666 | 20.600 | 1.499 | 50.666 | 20.600 | 1.499 |
| 8 | 45.818 | 23.113 | 1.161 | 45.825 | 23.118 | 1.154 |
| 9 | 52.260 | 35.066 | 1.209 | 52.264 | 35.068 | 1.206 |
| 10 | 56.798 | 32.266 | 1.472 | 56.800 | 32.266 | 1.471 |
| 11 | 62.207 | 42.516 | 1.410 | 62.207 | 42.516 | 1.410 |
| 12 | 57.370 | 44.936 | 1.194 | 57.370 | 44.936 | 1.194 |
| 13 | 63.786 | 57.144 | 0.983 | 63.786 | 57.144 | 0.983 |
| 14 | 68.547 | 54.632 | 1.120 | 68.547 | 54.632 | 1.120 |
| 15 | 73.594 | 64.568 | 0.763 | 73.599 | 64.574 | 0.755 |
| 16 | 69.256 | 67.529 | 0.659 | 69.263 | 67.537 | 0.648 |
| 17 | 74.982 | 77.865 | 0.137 | 74.991 | 77.877 | 0.127 |
| 18 | 79.289 | 75.521 | 0.263 | 79.293 | 75.528 | 0.257 |
| | Third Measurement | | | Fourth measurement | | |
| PN | E(m) | N(m) | U(m) | E(m) | N(m) | U(m) |
| 1 | 23.022 | 0.395 | 1.509 | 23.030 | 0.403 | 1.500 |
| 2 | 27.260 | 4.005 | 0.985 | 27.264 | 4.000 | 0.981 |
| 3 | 35.031 | 1.128 | 1.173 | 35.036 | 1.132 | 1.169 |
| 4 | 31.530 | 5.466 | 0.866 | 31.538 | 5.474 | 0.857 |
| 5 | 40.211 | 13.968 | 1.016 | 40.219 | 13.976 | 1.009 |
| 6 | 44.383 | 10.635 | 1.256 | 44.386 | 10.635 | 1.252 |
| 7 | 50.669 | 20.603 | 1.497 | 50.673 | 20.605 | 1.493 |
| 8 | 45.834 | 23.124 | 1.146 | 45.841 | -23.131 | 1.138 |
| 9 | 52.269 | 35.072 | 1.200 | 52.272 | 35.076 | 1.195 |
| 10 | 56.804 | 32.269 | 1.466 | 56.808 | 32.273 | 1.464 |
| 11 | 62.207 | 42.516 | 1.407 | 62.210 | 42.518 | 1.404 |
| 12 | 57.372 | -44.939 | 1.189 | 57.377 | 44.943 | 1.183 |
| 13 | 63.791 | 57.149 | 0.976 | 63.796 | 57.155 | 0.970 |
| 14 | 68.550 | 54.634 | 1.115 | 68.551 | 54.634 | 1.113 |
| 15 | 73.604 | 64.579 | 0.749 | 73.606 | 64.584 | 0.745 |
| 16 | 69.270 | 67.544 | 0.640 | 69.279 | 67.553 | 0.632 |
| 17 | 74.999 | 77.886 | 0.118 | 75.006 | 77.894 | 0.108 |
| 18 | 79.297 | 75.534 | 0.251 | 79.301 | 75.540 | 0.246 |

*Note. Per-epoch ENU coordinates (E, N, U) are given in meters and rounded to 0.001 m. WGS 84 / UTM Zone 34N (EPSG: 32634) is used only for mapping and not in the ENU calculation. Sub-millimeter changes between consecutive observations may be hidden by rounding; see Table 4 for inter-epoch differences.*

Reference frames and units. Mapping coordinates are associated with WGS 84 / UTM Zone 34N (EPSG: 32634) solely for cartographic visualization purposes and are not used in ENU calculations. Per-epoch ENU positions are recorded in meters and exported to three decimal places (0.001 m) for data provenance and reproducibility; they do not indicate measurement accuracy. Inter-epoch differences at each station, ΔE, ΔN, and ΔU, are expressed in millimeters relative to the baseline epoch (3 May 2024), with the sign convention: +E east, +N north, and +U upward. Station-level ENU values (meters) are provided in Table 4, while inter-epoch differences (millimeters) are summarized in Table 5. Units are clearly indicated in all tables, axes, and captions.

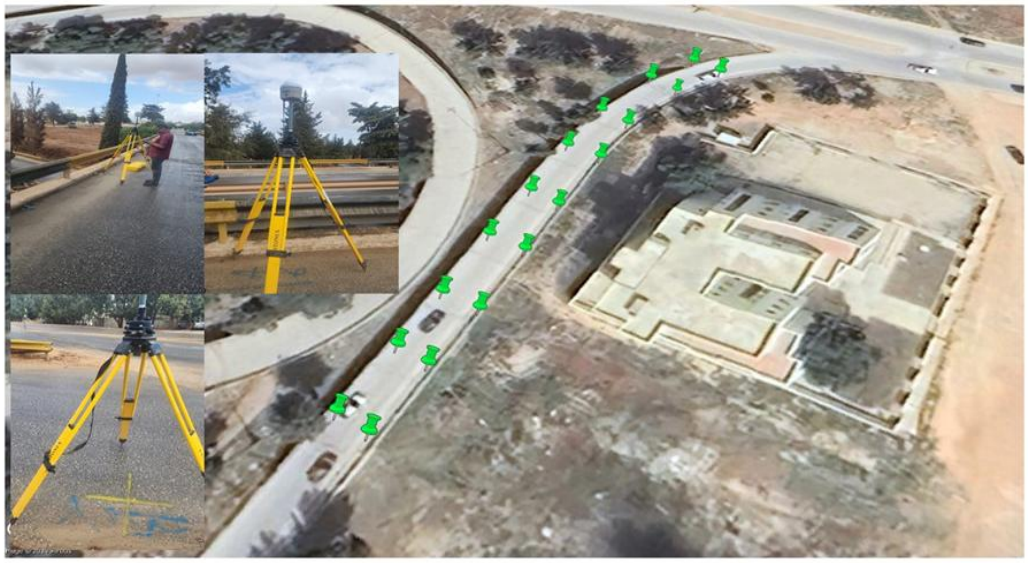

Fig. 5. The nine measurement locations on the right and left sides of the bridge

Temporal deformation was assessed by comparing endpoint differences over the monitoring period, with May 3, 2024, serving as the baseline and November 4, 2024, as the endpoint. For each station, displacements ΔE, ΔN, and ΔU were calculated within the local ENU coordinate system and expressed in millimeters (mm), converted from meter-scale coordinates to represent the observed millimeter-level variations accurately. The station-specific results are presented in Table 5 (mm). To ensure data reliability, campaign-level acquisition metrics are included, such as fix ratios, PDOP statistics, satellite counts, and the percentage of high-PDOP epochs excluded in accordance with policy. Utilizing R1 as the reference station and maintaining a consistent station setup across epochs provided a uniform baseline geometry, thereby facilitating direct temporal comparisons.

Table 5. Endpoint displacements in local ENU relative to the 3 May 2024 baseline

| PN | ΔE (mm) | ΔN (mm) | ΔU (mm) |
|---|---|---|---|
| 1 | 27 | 22 | 25 |
| 2 | 14 | 13 | 21 |
| 3 | 11 | 13 | 15 |
| 4 | 25 | 24 | 28 |
| 5 | 24 | 22 | 21 |
| 6 | 19 | 13 | 15 |
| 7 | 7 | 5 | 6 |
| 8 | 23 | 18 | 23 |
| 9 | 12 | 10 | 14 |
| 10 | 10 | 7 | 8 |
| 11 | 3 | 2 | 6 |
| 12 | 7 | 7 | 11 |
| 13 | 10 | 11 | 13 |
| 14 | 4 | 2 | 7 |
| 15 | 12 | 16 | 18 |
| 16 | 23 | 24 | 27 |
| 17 | 24 | 29 | 29 |
| 18 | 12 | 19 | 17 |

*Note. Inter-epoch differences are reported in millimeters relative to the baseline epoch (May 3, 2024). Values less than 0.5 mm are rounded to 0 mm. Differences within the method's practical repeatability (approximately 4–6 mm horizontally; approximately 7–12 mm vertically) are not considered significant motion.*

### 2.4.3 Per-Station Acquisition Metadata and Session-Level Quality Metrics

To ensure transparency and reproducibility, the acquisition settings and key quality metrics for each station are systematically documented in Tables 6 through 9 for each field campaign: Campaign 1 on May 3, 2024; Campaign 2 on July 3, 2024; Campaign 3 on September 4, 2024; and Campaign 4 on November 4, 2024. Each table provides detailed information for stations PN1–PN19, including the antenna pole height, solution status, session-level median DOP indicators (PDOP, HDOP, VDOP), the median number of tracked satellites, the local date and start and end times, session duration, and receiver model. The baseline entry (PN1 used as the control) is designated as BASE (reference; DOP/Sats not applicable) because per-epoch rover quality indicators are not relevant to the reference station. All sessions were conducted using a dual-frequency STONEX S10 receiver operating at 1 Hz, with an elevation mask set at 15°, and exclusively fixed-ambiguity RTK epochs were permitted. Coordinates were recorded in WGS 84 / UTM zone 34N (EPSG: 32634), and all times are presented in local time (LT) using a 24-hour format. Session durations were approximately 15 minutes, with a range from 14 to 16 minutes across the campaigns.

Table 6. Per-station acquisition metadata and session-level quality metrics (Campaign 1, May 3, 2024)

| PN | Pole h. (m) | Status | PDOP | HDOP | VDOP | Sats (med) | Start–End (LT) |
|---|---|---|---|---|---|---|---|
| 1 | 1.86 | BASE | - | - | - | - | 06:34–06:49 |
| 2 | 1.70 | FIXED | 2.9 | 1.2 | 2.1 | 10 | 07:07–07:22 |
| 3 | 1.70 | FIXED | 2.1 | 1.1 | 1.8 | 12 | 07:24–07:39 |
| 4 | 1.70 | FIXED | 2.1 | 1.1 | 1.8 | 12 | 07:54–08:09 |
| 5 | 1.70 | FIXED | 2.9 | 1.2 | 2.7 | 11 | 08:28–08:43 |
| 6 | 1.70 | FIXED | 2.1 | 1.1 | 1.8 | 12 | 08:59–09:14 |
| 7 | 1.70 | FIXED | 2.6 | 1.3 | 2.3 | 9 | 09:24–09:39 |
| 8 | 1.70 | FIXED | 3.4 | 1.3 | 2.0 | 10 | 09:51–10:06 |
| 9 | 1.70 | FIXED | 2.9 | 1.1 | 2.0 | 12 | 10:23–10:38 |
| 10 | 1.70 | FIXED | 2.9 | 1.2 | 2.1 | 11 | 10:52–11:07 |
| 11 | 1.70 | FIXED | 2.9 | 1.2 | 2.3 | 11 | 11:27–11:42 |
| 12 | 1.70 | FIXED | 3.0 | 1.2 | 2.0 | 11 | 11:59–12:14 |
| 13 | 1.70 | FIXED | 3.0 | 1.3 | 2.2 | 10 | 13:29–13:44 |
| 14 | 1.70 | FIXED | 2.1 | 1.1 | 1.8 | 12 | 13:55–14:10 |
| 15 | 1.70 | FIXED | 2.1 | 1.1 | 1.8 | 12 | 14:27–14:42 |
| 16 | 1.70 | FIXED | 2.2 | 1.1 | 1.9 | 12 | 15:44–15:59 |
| 17 | 1.70 | FIXED | 2.1 | 1.1 | 1.8 | 12 | 16:16–16:31 |
| 18 | 1.70 | FIXED | 2.5 | 1.4 | 2.1 | 9 | 16:44–16:59 |
| 19 | 1.70 | FIXED | 2.3 | 1.1 | 2.1 | 11 | 17:26–17:41 |

*Notes: Coordinates are provided in the WGS 84 / UTM zone 34N coordinate system (EPSG:32634). Observations were collected using a STONEX S10 receiver, with data sampled at 1 Hz and an elevation mask set at 15°. Only epochs with fixed-ambiguity RTK solutions are included. The session durations for this campaign are 15 minutes, ranging from 14 to 16 minutes across different campaigns. Times are expressed in local (24-hour) format.*

Table 7. Per-station acquisition metadata and session-level quality metrics (Campaign 2, July 3, 2024)

| PN | Pole h. (m) | Status | PDOP (med) | HDOP | VDOP | Sats (med) | Start–End (LT) |
|---|---|---|---|---|---|---|---|
| 1 | 2.15 | BASE | - | - | - | - | 05:10–05:25 |
| 2 | 1.90 | FIXED | 1.9 | 1.0 | 2.0 | 10 | 05:57–06:12 |
| 3 | 1.90 | FIXED | 2.3 | 1.3 | 2.0 | 12 | 06:29–06:44 |
| 4 | 1.90 | FIXED | 2.2 | 1.0 | 2.1 | 12 | 06:59–07:14 |
| 5 | 1.90 | FIXED | 2.6 | 1.3 | 2.5 | 11 | 07:24–07:39 |
| 6 | 1.90 | FIXED | 1.9 | 1.2 | 2.2 | 12 | 07:50–08:05 |
| 7 | 1.90 | FIXED | 2.9 | 1.4 | 2.1 | 9 | 08:20–08:35 |
| 8 | 1.90 | FIXED | 3.0 | 1.2 | 2.3 | 10 | 08:47–09:02 |
| 9 | 1.90 | FIXED | 2.8 | 1.3 | 2.0 | 12 | 09:18–09:33 |

| | | | | | | | |
|---|---|---|---|---|---|---|---|
| 10 | 1.90 | FIXED | 2.8 | 1.1 | 2.4 | 11 | 09:47–10:02 |
| 11 | 1.90 | FIXED | 2.8 | 1.3 | 2.1 | 11 | 10:14–10:29 |
| 12 | 1.90 | FIXED | 2.8 | 1.1 | 2.1 | 11 | 10:40–10:55 |
| 13 | 1.90 | FIXED | 2.8 | 1.2 | 2.1 | 10 | 11:11–11:26 |
| 14 | 1.90 | FIXED | 2.8 | 1.3 | 2.1 | 12 | 14:05–14:20 |
| 15 | 1.90 | FIXED | 2.0 | 1.2 | 2.1 | 12 | 14:34–14:49 |
| 16 | 1.90 | FIXED | 2.4 | 1.1 | 1.2 | 12 | 14:58–15:13 |
| 17 | 1.90 | FIXED | 1.9 | 1.1 | 1.7 | 12 | 15:32–15:47 |
| 18 | 1.90 | FIXED | 2.0 | 1.2 | 2.0 | 9 | 16:06–16:21 |
| 19 | 1.90 | FIXED | 2.7 | 1.1 | 2.2 | 11 | 16:40–16:55 |

*Notes: Coordinates are given in WGS 84 / UTM zone 34N (EPSG:32634). Observations were collected using a STONEX S10 receiver, with data sampled at 1 Hz and an elevation mask of 15°. Only epochs with fixed-ambiguity RTK solutions were used. The session durations for this survey were 15 minutes. DOP and satellite data are based on median values per station session. Times are in local (24-hour) format.*

Table 8. Per-station acquisition metadata and session-level quality metrics (Campaign 3, September 4, 2024)

| PN | Pole h. (m) | Status | PDOP (med) | HDOP | VDOP | Sats (med) | Start–End (LT) |
|---|---|---|---|---|---|---|---|
| 1 | 2.05 | BASE | - | - | - | - | 05:30–05:45 |
| 2 | 1.80 | FIXED | 1.9 | 1.2 | 2.0 | 11 | 06:05–06:20 |
| 3 | 1.80 | FIXED | 2.0 | 1.2 | 2.0 | 11 | 06:37–06:52 |
| 4 | 1.80 | FIXED | 2.0 | 1.0 | 1.7 | 11 | 07:10–07:25 |
| 5 | 1.80 | FIXED | 2.0 | 1.3 | 1.9 | 11 | 07:33–07:48 |
| 6 | 1.80 | FIXED | 2.0 | 1.3 | 1.6 | 10 | 08:09–08:24 |
| 7 | 1.80 | FIXED | 2.1 | 1.5 | 1.3 | 11 | 08:39–08:54 |
| 8 | 1.80 | FIXED | 1.9 | 1.3 | 2.0 | 12 | 09:06–09:21 |
| 9 | 1.80 | FIXED | 2.0 | 1.1 | 2.0 | 10 | 09:33–09:48 |
| 10 | 1.80 | FIXED | 2.3 | 1.1 | 2.0 | 12 | 10:12–10:27 |
| 11 | 1.80 | FIXED | 2.2 | 1.6 | 2.0 | 12 | 10:35–10:50 |
| 12 | 1.80 | FIXED | 2.2 | 1.2 | 2.0 | 12 | 11:13–11:28 |
| 13 | 1.80 | FIXED | 2.2 | 1.2 | 1.9 | 12 | 11:40–11:55 |
| 14 | 1.80 | FIXED | 1.9 | 1.2 | 1.9 | 12 | 12:07–12:22 |
| 15 | 1.80 | FIXED | 2.0 | 1.0 | 1.9 | 11 | 13:03–13:18 |
| 16 | 1.80 | FIXED | 2.4 | 1.3 | 2.0 | 9 | 13:31–13:46 |
| 17 | 1.80 | FIXED | 1.9 | 1.2 | 1.7 | 10 | 14:07–14:22 |
| 18 | 1.80 | FIXED | 2.0 | 1.0 | 2.0 | 10 | 14:40–14:55 |
| 19 | 1.80 | FIXED | 2.0 | 1.4 | 2.2 | 12 | 15:19–15:34 |

*Notes: Coordinates are in WGS 84 / UTM zone 34N (EPSG:32634). Observations were taken with a STONEX S10 receiver, sampling at 1 Hz with a 15° elevation mask. Only fixed-ambiguity RTK epochs were included. Each ession lasted 15 minutes during this campaign. DOP and satellite values are median values per station session. Times are local (24-hour).*

Table 9. Per-station acquisition metadata and session-level quality metrics (Campaign 4, 2024-11-04)

| PN | Pole h. (m) | Status | PDOP (med) | HDOP | VDOP | Sats(med) | Start–End (LT) |
|---|---|---|---|---|---|---|---|
| 1 | 2.00 | BASE | - | - | - | - | 05:01–05:16 |
| 2 | 1.68 | FIXED | 2.0 | 1.1 | 2.1 | 9 | 05:28–05:43 |
| 3 | 1.68 | FIXED | 1.8 | 1.0 | 1.9 | 10 | 06:02–06:17 |
| 4 | 1.68 | FIXED | 2.0 | 1.4 | 2.0 | 10 | 06:34–06:49 |
| 5 | 1.68 | FIXED | 2.1 | 1.5 | 2.2 | 12 | 07:03–07:18 |
| 6 | 1.68 | FIXED | 1.9 | 1.2 | 1.7 | 9 | 07:36–07:51 |
| 7 | 1.68 | FIXED | 1.9 | 1.3 | 1.8 | 11 | 08:03–08:18 |
| 8 | 1.68 | FIXED | 1.9 | 1.2 | 2.1 | 9 | 08:31–08:46 |
| 9 | 1.68 | FIXED | 1.9 | 1.2 | 1.9 | 12 | 09:05–09:20 |

| | | | | | | | |
|---|---|---|---|---|---|---|---|
| 10 | 1.68 | FIXED | 2.1 | 1.3 | 2.1 | 10 | 09:37–09:52 |
| 11 | 1.68 | FIXED | 1.8 | 1.1 | 2.0 | 10 | 10:11–10:26 |
| 12 | 1.68 | FIXED | 2.0 | 1.5 | 1.6 | 10 | 10:42–10:57 |
| 13 | 1.68 | FIXED | 2.2 | 1.4 | 2.0 | 11 | 12:27–12:42 |
| 14 | 1.68 | FIXED | 2.0 | 1.4 | 1.9 | 12 | 12:59–01:14 |
| 15 | 1.68 | FIXED | 2.3 | 1.0 | 1.8 | 9 | 13:30–13:45 |
| 16 | 1.68 | FIXED | 2.0 | 1.3 | 2.0 | 9 | 14:06–14:21 |
| 17 | 1.68 | FIXED | 1.8 | 1.0 | 2.0 | 10 | 14:38–14:53 |
| 18 | 1.68 | FIXED | 2.0 | 1.1 | 2.0 | 9 | 15:20–15:35 |
| 19 | 1.68 | FIXED | 1.9 | 1.2 | 1.9 | 11 | 15:57–16:12 |

*Notes: Coordinates are provided in WGS 84 / UTM zone 34N (EPSG:32634). Observations were obtained using a STONEX S10 receiver, sampled at 1 Hz with an elevation mask set at 15°. Only epochs with fixed-ambiguity RTK solutions were included. The duration of sessions ranged from 14 to 16 minutes, as detailed. DOP and Satellite values represent the median per station. Times are recorded in local (24-hour) format.*

### *2.4.3 Data Quality Control and Uncertainty Quantification*

All acquisitions underwent thorough quality control. Only epochs fixed with integers were included in the solution; any epoch with PDOP over 4, satellite elevation below 15°, non-fixed ambiguities, or an unresolved cycle-slip/loss of lock was rejected. Antenna model and height were consistently recorded, and instrument centering was verified with bipod/tribrach checks to minimize setup bias. Before each RTK campaign, the local datum was established by observing the SDL control marks R1 and R2 in sessions lasting at least 40 minutes, followed by a minimally constrained least-squares adjustment to verify mark stability and propagate control variances. The adjusted control demonstrated sub-centimeter stability; its contribution to the displacement budget is estimated to be less than 2 mm horizontally and less than 3 mm vertically in the ENU frame, anchored at R1. This control realization is performed once per campaign and does not need to be repeated elsewhere in the Methods.

Table 10. Campaign-level RTK quality summary

| Campaign (2024) | Fix (epochs/total, %) | PDOP (min/median/max) | Sats (median/range) | PDOP>4 (Epochs, %) | QC status |
|---|---|---|---|---|---|
| May 3 | 110 / 111 = 99.1% | 1.257 / 1.708 / 6.119 | 13 / 5–16 | 4 / 111 = 3.6% | PASS |
| Jul 3 | 116 / 117 = 99.1% | 1.29 / 1.77 / 5.10 | 13 / 6–17 | 2 / 117 = 1.7% | PASS |
| Sep 3 | 134 / 135 = 99.3% | 1.22 / 1.66 / 4.75 | 14 / 7–17 | 1 / 135 = 0.7% | PASS |
| Nov 4 | 97 / 98 = 99.0% | 1.36 / 1.83 / 5.25 | 12 / 6–16 | 3 / 98 = 3.1% | PASS |

*Notes (Table 10): PDOP is a dimensionless quantity; "Satellites" refers to a count; "PDOP>4" indicates the percentage of epochs omitted by policy; "Fix (epochs/total, %)" displays both the count and percentage. ENU displacements elsewhere are expressed in millimeters.*

Acquisition diagnostics aligned with short-baseline RTK under low-multipath conditions: fix ratios ranged from 99.0 to 99.3%; median PDOP was between 1.66 and 1.83; and the median number of tracked satellites was 12 to 14 (overall 5 to 17). High-PDOP rejections were minimal (0.7 to 3.6% of epochs), indicating stable geometry across occupations and supporting millimeter-scale differencing in the local frame. The station-level error budget is primarily influenced by the stochastic positioning noise of fixed RTK over approximately fifteen-minute dwell periods, amounting to approximately 3–5 mm in the horizontal plane and 5–10 mm in the vertical direction. Minor systematic errors originate from the antenna phase center and height, estimated at 1–2 mm, as well as from instrument or mark centering, also estimated at 1–2 mm. Residual multipath effects and atmospheric influences persist at a scale of a few millimeters, further mitigated by the use of short baselines and common-mode cancellation techniques. The control realization obtained from the R1/R2 static adjustment contributes to less than 2 mm horizontally and less than 3 mm vertically. By treating components as independent variables and aggregating their impacts in

quadrature, the practical repeatability is approximately 4–6 mm in planimetric coordinates and roughly 7–12 mm in height. These parameters serve to inform the interpretation of endpoint-to-baseline ENU displacements as detailed in Table 10.

#### *2.4.4 Detectability Thresholds and Statistical Significance of Displacements*

Uncertainty was assessed for each station and component (ΔE, ΔN, ΔU) by analyzing dispersion within a session of accepted fixed-ambiguity RTK solutions (at 1 Hz). This analysis utilized a straightforward correction for temporal correlation, incorporating an appropriate sample size. The variation in the endpoint between sessions (e.g., epoch 4 versus epoch 1) was subsequently compared to a 95% minimal-detectable shift to differentiate noise-like fluctuations from statistically significant signals. The primary estimators and the 95% detectability criterion are provided below, with the following notation defined. Session-level standard error:

$$SE_{session} = \frac{\sigma_{epoch}}{\sqrt{N_{eff}}} \quad (reducing\ to\ \sigma_{epoch}/\sqrt{N}\ if\ \rho_1 \approx 0) \tag{1}$$

Endpoint-change uncertainty (error propagation):

$$SE_{\Delta} = \sqrt{SE_4^2 + SE_1^2} \tag{2}$$

The 95% minimal-detectable quasi-static shift is $\tau_{95} = k\,\mathrm{SE}_{\Delta}$, $k = 1.96$ (large samples) or $k = t_{0.975,\nu}$ for small. $N_{\mathrm{eff}}$

The decision criterion specifies that a change is considered statistically detectable (structural) if $|\Delta| > \tau_{95}$; otherwise, it is classified as noise consistent. To mitigate the incidence of false alarms, detectability further requires persistence across at least two consecutive epochs (for example, exceeding thresholds in both 1 to 3 and 1 to 4).

Where;$\sigma_{\mathrm{epoch}}$ denotes the dispersion of accepted fixed RTK solutions within a session, measured at a frequency of 1 Hz. $N_{\mathrm{eff}}$ signifies the adequate sample size that compensates for serial correlation, diminishing to N when correlation effects are negligible. $\mathrm{SE}_1$ and $\mathrm{SE}_4$ represent the session-level standard errors for the baseline (epoch 1) and the endpoint (epoch 4), respectively. $\mathrm{SE}_{\Delta}$ indicates the standard error associated with the change at the endpoint. The coverage factor k is set to 1.96 for large effective samples, or the appropriate Student's t critical value $t_{0.975,\nu}$ when $N_{\mathrm{eff}}$ is small.

In the absence of station-specific within-session statistics, conservative network-level repeatability bands (e.g., horizontal $\tau_{95}$,h ≈ 6 mm; vertical $\tau_{95}$,v ≈ 12 mm) are employed as surrogate detectability thresholds and are applied using the same decision rule.

### 2.5. GIS-Based Visualization and Tabulation of ENU Displacements

Contemporary methodologies for Structural Health Monitoring (SHM) of bridges increasingly incorporate tabular data alongside Geographic Information Systems (GIS) to convert station-based GNSS solutions into standardized summaries across units, thereby preserving spatial coherence and facilitating engineering analysis. Spreadsheet layers, such as those in Excel, offer transparent quality control, enable comparisons over different periods, and provide easily accessible tables. Simultaneously, GIS delineates structural boundaries, including deck masks, and generates publication-quality maps that illustrate gradients at the deck level, features that are often not discernible solely through time-series data. Additionally, digital twin research illustrates that integrating carefully selected sensor data with spatial models improves decision-making and reduces uncertainty in displacement analysis at the asset level [33]. During spatial mapping, deterministic, distance-weighted interpolation remains a reliable and comprehensible method at moderate station densities, provided that parameters such as neighborhood size, power, and masking are precisely calibrated to the structure [34]. Recent advancements in GIS emphasize the importance of rigorous data preparation and visualization standards, which are essential for credible spatial analysis and effective communication with stakeholders. The existing Excel-to-GIS workflow inherently supports these standards.

Excel was employed to facilitate secure unit management, ensure reproducible quality control filters, and generate journal-ready tables and figures that are directly traceable to raw station solutions. ArcGIS was utilized to (i) restrict interpolation and visualization to the bridge deck through polygon masking, (ii) preserve the accuracy of the Coordinate Reference System (CRS) and associate transformations (WGS-84/UTM to ENU), and (iii) export cartographic layouts at specified scales with embedded fonts and comprehensive unit legends. A comparable methodology, integrating spreadsheet-based quality control with GIS-enabled domain control and mapping, has been documented in recent scholarly literature and conforms to established reporting standards within the domain of structural health monitoring.

The local ENU components (ΔE, ΔN, ΔU) for each station and observation period were consolidated into a single workbook with standardized units. Values were converted to millimeters before analysis to ensure consistency in reporting scales across all calculations and figures. Following quality screening, fixed-ambiguity solutions were retained, and epochs exhibiting low reliability (PDOP ≤ 4) were excluded. Subsequently, Excel was utilized to derive base-referenced contrasts that elucidate temporal variations at the station level. The contrasts are expressed as.

$$\Delta^{(2-1)}X,\ \Delta^{(3-1)}X,\ \Delta^{(4-1)}X \quad for\, X \in \{E_{mm},\ N_{mm},\ U_{mm}\} \tag{3}$$

Where;

- $X \in \{E_{\mathrm{mm}}, N_{\mathrm{mm}}, U_{\mathrm{mm}}\}$ : local ENU components expressed in millimetres.
- $E_{\mathrm{mm}}$ : east displacement (mm) in the local ENU frame.
- $N_{\mathrm{mm}}$ : north displacement (mm) in the local ENU frame.
- $U_{\mathrm{mm}}$ : up/vertical displacement (mm) in the local ENU frame.

These differences were subsequently presented as three-line charts for each component, utilizing standardized axes and explicit unit labels (mm) to enhance understanding. The visual summaries offer a concise overview of short-, medium-, and long-term drift within each component, thereby serving as an intermediary between raw GNSS outputs and subsequent structural analysis. They adhere to established best practices in pattern recognition-focused Structural Health Monitoring (SHM) reporting, emphasizing transparent data preprocessing and clear, unit-specific summaries.

Interpolation constitutes a fundamental methodology within the domain of spatial structural diagnostics, facilitating the transformation of sparse measurement data into continuous fields across structural components [35]. This methodology supports the identification of critical responses and spatial gradients that might otherwise remain concealed within station-based time series. In the context of bridge structural health monitoring (SHM), such spatial visualizations serve as supplementary instruments complementing traditional time-series analysis and pattern recognition, by revealing deck-wide patterns that are not immediately discernible within individual sensor data [36-37]. Both geostatistical and deterministic interpolators provide controlled generalizations from discrete observations to the entire structure, thereby improving interpretability for engineers. A comprehensive body of literature in environmental and engineering Geographic Information Systems (GIS) affirms that deterministic, distance-based interpolators ,including inverse distance weighting (IDW), are capable of producing stable and transparent surface models at moderate sampling densities for smoothly varying fields [38-39]. Recent investigations suggest that distance-informed methods remain effective for terrains or topologically constrained issues when neighborhoods, masking, and scales are explicitly designed, exemplified by topography-aware inverse-radius weighting [40]. Consequently, selected stations were incorporated into the GIS and stored within a file geodatabase, with the bridge-deck polygon delineating the analysis region. RTK measurements along the bridge, represented as point features, are illustrated in Fig. 6, demonstrating the station configuration employed in subsequent spatial analysis. All raster operations were confined within the deck area to prevent extrapolation beyond the structure's footprint. A grid resolution of approximately 0.25 meters was selected to sufficiently capture the spatial wavelengths at the deck level, thereby avoiding unnecessary over-refinement relative to station spacing.

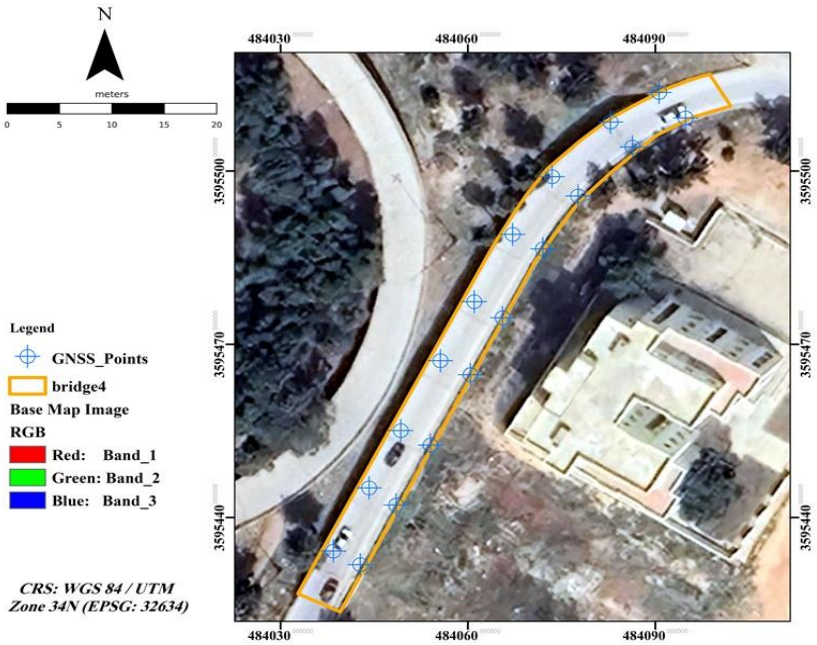


Fig. 6. Real-Time Kinematic (RTK) measurements along the bridge

Interpolation of displacement fields (IDW) was undertaken only where spatial synthesis was informative (e.g., deck-wide patterns of $U_{mm}$). The estimator adopted a classical inverse-distance form, stated here as

$$\hat{Z}(s_0) = \frac{\sum_{i=1}^{N} w_i Z(s_i)}{\sum_{i=1}^{N} w_i} \tag{4}$$

Where; $\hat{Z}(s_0)$: The estimated value at the unknown location $s_0$, $Z(s_i)$: The observed value at the known location $s_i$, $N$: The number of known points used for interpolation, $w_i$: The weight assigned to each known point $s_i$, calculated as:

$$w_i = \frac{1}{d(s_0, s_i)^p} \tag{5}$$

Where; $d(s_0, s_i)$: The distance between the unknown point $s_0$ and the known point $s_i$, $p$: The power parameter, which controls the influence of distance on the weights.

Typical values include:

- $p$ = 1: Produces a smoother interpolation with a broader influence.
- $p$ = 2: The most commonly used value, giving more weight to closer points.
- $p$ > 2: Strongly reduces the influence of distant points

A power parameter of p = 2 was selected to prioritize nearby evidence while maintaining estimator stability across the deck and empirically calibrated s, for Inverse Distance Weighting (IDW), which reduces noise amplification compared to higher exponents [41]. Conversely, p = 1 yields a smoother field suitable for gentle gradients, while p > 2 offers robust localization, especially useful for sharp spatial contrasts. A variable neighborhood, limited to 12 stations, was employed to manage extrapolative influence under moderate sensor densities and to mitigate sensitivity to irregular sampling, in accordance with current guidelines on neighborhood setup in deterministic spatial interpolation [42]. Interpolation was confined to the bridge deck domain to restrict estimates to the structural surface and minimize edge artifacts, aligning the computation with the local East-North-Up (ENU) plane and recent distance-aware, locally adaptive techniques used in engineering geospatial practice [43]. A grid resolution of approximately 0.25 meters was chosen to correspond with the smallest structurally interpretable features at the deck level, while avoiding over-refinement relative to station spacing.

Cartographic products were created at fixed layout scales, including the following elements: (i) a simple north arrow, (ii) a clearly marked scale bar, (iii) a neat line without graticules, and (iv) legends explicitly indicating units (mm). Continuous rasters used nine perceptually ordered classes with documented class-break logic, based on either equal-interval or quantile schemes. Final output was exported at 600 dpi with embedded fonts to ensure print-quality resolution and consistent reproduction. Geodetic transformations and reference realizations were performed before this stage. Excel was used for unit-safe data management and cross-epoch statistical comparisons, while the GIS environment handled domain-controlled interpolation and publication-quality cartography within the local ENU frame. This methodological segmentation guarantees transparency and reproducibility, leveraging the unique advantages of each tool.

### *2.5.1 IDW Cross-Validation and Parameter Sensitivity*

The accuracy and reliability of the interpolation were assessed using a leave-one-out cross-validation (LOOCV) method, applied to a limited set of Inverse Distance Weighting (IDW) parameters. For each station $i = 1, ..., n$, the observed endpoint displacement $z_{ni}$ (related to a specific component ΔE, ΔN, ΔU measured in millimeters) was removed and then estimated using the remaining stations with the chosen IDW parameters, with station i excluded from the neighborhood. Planar distances for the k-Nearest Neighbors (k-NN) search were calculated within a unified metric space based on first-epoch UTM coordinates. The parameter grid included p ∈ {1, 2, 3} and k ∈ {6, 12}. The following equations are used to perform and evaluate this process.

Distance metric (UTM plane):

$$d(x_i, x_j) = \sqrt{(x_i - x_j)^2 + (y_i - y_j)^2} \tag{6}$$

IDW prediction (point withheld in LOOCV):

$$\widehat{z_i} = \frac{\sum_{j=1}^{m} d(x_i, x_j)^{-p} z_j}{\sum_{j=1}^{m} d(x_i, x_j)^{-p}} \tag{7}$$

Error metrics: Root Mean Square Error and Mean Absolute Error

$$\text{RMSE} = \sqrt{\frac{1}{n}\sum_{i=1}^{n}(z_i - \widehat{z_i})^2} \tag{8}$$

$$MAE = \frac{1}{n}\sum_{i=1}^{n} / z_i - \widehat{z_i} / \tag{9}$$

Where; n: number of stations (points), $(x_i, y_i)$ UTM coordinates of station i (meters) from (first epoch), $d(x_i, x_j)$: Euclidean distance in metres between stations i and j, $z_i$: observed displacement at station i (ΔE, ΔN, or ΔU; millimetres), endpoint difference relative to 3 May 2024, p: distance-decay exponent (tested values: 1, 2, 3), k: neighborhood size (tested values: 6, 12), $\widehat{z_i}$: IDW-predicted value at station i using the current (p, k).

The Root Mean Square Error (RMSE) and the Mean Absolute Error (MAE) are calculated using residuals obtained from Leave-One-Out Cross-Validation, with measurements expressed in millimeters.

- Hotspot-stability (rank agreement): The stability of hotspot locations was further evaluated to test their robustness against different parameter choices. Spearman's rank correlation coefficient (ρ) was calculated between the leave-one-out cross-validation (LOOCV) predicted vectors for each (p, k) and the baseline setup, aiming to measure how well the station-wise intensity rankings were preserved.
- Edge effects, outliers, and selection: Neighborhood sizes (k) were restricted based on network density to reduce boundary artifacts. Absolute LOOCV residuals were examined for

disproportionate outlier influence; no data points were excluded unless supported by acquisition-quality indicators. The best (p, k) combination was selected to minimize RMSE/MAE while ensuring high rank agreement across different settings.

## 3. Results and Discussions

### 3.1. Bridge Displacement Results Across Four Epochs

The data provides valuable insights into the structural behavior of the bridge at various points, illustrating changes in Easting (ΔE), Northing (ΔN), and Height (ΔU) across three observation periods. The recorded variations will be systematically analyzed to identify significant shifts and ascertain their directions. Comparisons are conducted between three pairs of observations: Observation (1) and (2), Observation (1) and (3), and Observation (1) and (4). Each point (PN) signifies differences in three dimensions, reflecting the extent of positional changes over time. Most locations exhibit a trend of increasing displacement as the observations progress, indicating ongoing structural movement, as summarized in Table 11.

Table 11. Important information on the bridge's structural behavior at different points

| | Difference Calculations | | | | | | | | |
|---|---|---|---|---|---|---|---|---|---|
| | Observation (1) and (2) | | | Observation (1) and (3) | | | Observation (1) and (4) | | |
| PN | ΔE (mm) | ΔN (mm) | ΔU (mm) | ΔE (mm) | ΔN (mm) | ΔU (mm) | ΔE (mm) | ΔN (mm) | ΔU (mm) |
| 1 | 8 | 5 | 9 | 19 | 14 | 16 | 27 | 22 | 25 |
| 2 | 6 | 4 | 11 | 10 | 8 | 17 | 14 | 13 | 21 |
| 3 | 3 | 4 | 5 | 6 | 9 | 11 | 11 | 13 | 15 |
| 4 | 9 | 9 | 11 | 17 | 16 | 19 | 25 | 24 | 28 |
| 5 | 9 | 7 | 6 | 16 | 14 | 14 | 24 | 22 | 21 |
| 6 | 12 | 9 | 8 | 16 | 13 | 11 | 19 | 13 | 15 |
| 7 | 0 | 0 | 0 | 3 | 3 | 2 | 7 | 5 | 6 |
| 8 | 7 | 5 | 7 | 16 | 11 | 15 | 23 | 18 | 23 |
| 9 | 4 | 2 | 3 | 9 | 6 | 9 | 12 | 10 | 14 |
| 10 | 2 | 0 | 1 | 6 | 3 | 6 | 10 | 7 | 8 |
| 11 | 0 | 0 | 0 | 0 | 0 | 3 | 3 | 2 | 6 |
| 12 | 0 | 0 | 0 | 2 | 3 | 5 | 7 | 7 | 11 |
| 13 | 0 | 0 | 0 | 5 | 5 | 7 | 11 | 11 | 13 |
| 14 | 0 | 0 | 0 | 3 | 2 | 5 | 4 | 2 | 7 |
| 15 | 5 | 6 | 8 | 10 | 11 | 14 | 12 | 16 | 18 |
| 16 | 7 | 8 | 11 | 14 | 15 | 19 | 23 | 24 | 27 |
| 17 | 9 | 12 | 10 | 17 | 21 | 19 | 24 | 29 | 29 |
| 18 | 4 | 7 | 6 | 8 | 13 | 12 | 12 | 19 | 17 |

The graphs illustrate the variations in East (ΔE) measurements at various observation points on the Bridge in Al-Marj City, Libya. Three sets of (ΔE) observations are presented, identified as Observation (1) and (2), Observation (1) and (3), as well as Observation (1) and (4). The graphical data demonstrate notable fluctuations in (ΔE) values at different points, suggesting potential instability or inconsistency in structural behavior. Although the three datasets generally exhibit similar patterns, certain discrepancies in specific (ΔE) values at particular locations imply possible structural changes over time. Points exhibiting higher ΔE values, such as 1, 4, 5, 8, 16, and 17, indicate regions undergoing more substantial shifts or movements, which may necessitate further analysis or continuous monitoring. Conversely, points with lower (ΔE) values, including 7, 10, 11, 12, and 14, display minimal variation, signifying a relatively stable condition, as depicted in Fig. 7.

The differently colored lines represent three distinct sets of (ΔN) measurements, labeled as Observations (1) and (2), (1) and (3), and (1) and (4). The structural behavior toward the North demonstrates some instability and fluctuation over time, as evidenced by substantial variations in (ΔN) values across multiple observation points. Certain (ΔN) values at specific locations within the

three observation sets exhibit variability, implying that the structural behavior has likely undergone changes during the observation periods. Movements or shifts in the North direction are more evident at stations with higher (ΔN) values, such as stations 1, 4, 5, 1, 4, 5, 1,4,5,16, and 17. Conversely, sites with lower (ΔN) values, including stations 7, 9, 10, 11, 12, and 14, may experience less movement or structural alteration, as depicted in Fig. 8.

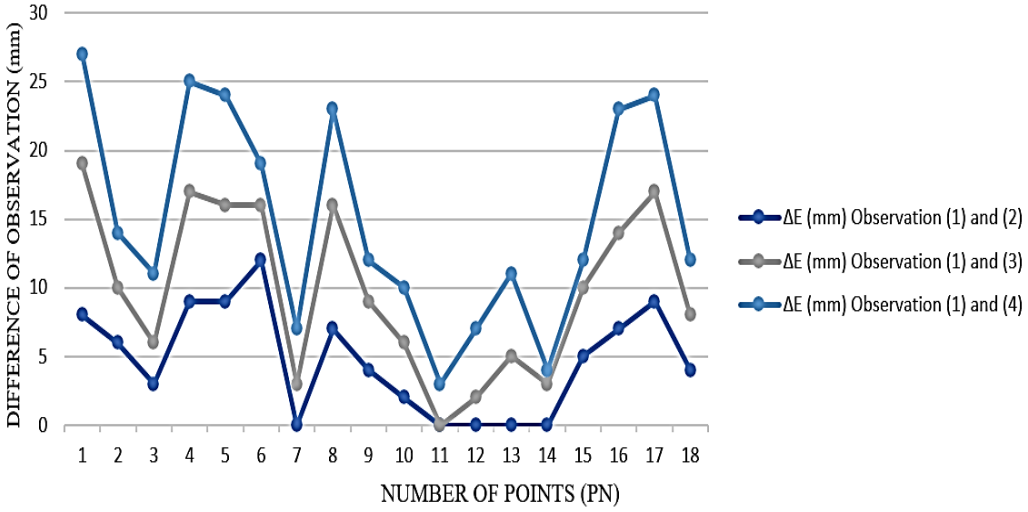


Fig. 7. Changes in East (ΔE) measurements

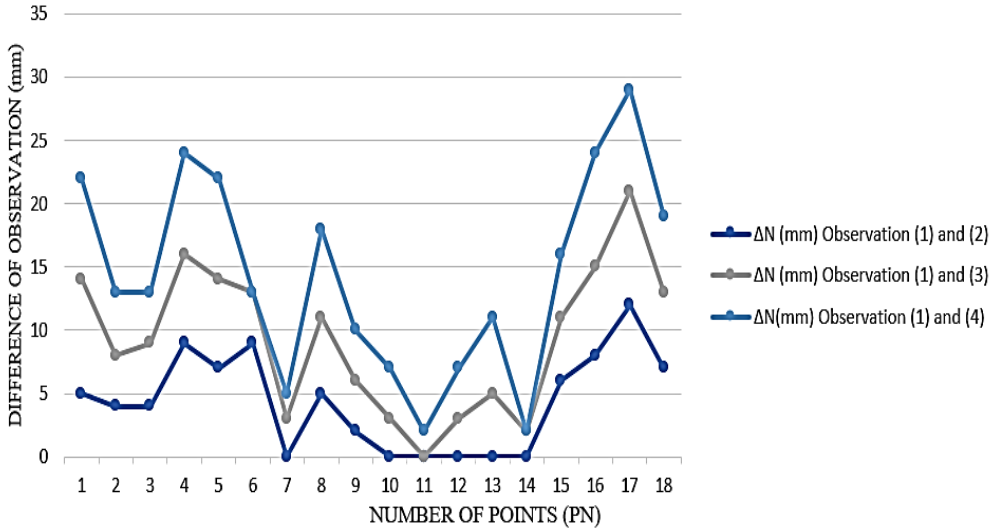


Fig. 8. Changes in North (Δ N) measurements

The vertical (ΔU) measurements of a bridge, recorded at multiple observation points (PN), are depicted in the accompanying graphs. Three distinct datasets, designated as Observation (1) and (2), Observation (1) and (3), as well as Observation (1) and (4), represent various sets of (Δ U) observations. Although these datasets exhibit similar overall trends, certain observation points display variations in the (Δ U) values, suggesting that the structural behavior has undergone changes or evolution across different observation periods. Notably, the (Δ U) measurements at specific points, such as 1, 2, 4, 5, 8, 16, and 17, are markedly higher than at other points, indicating regions with more pronounced vertical shifts or movements. Conversely, the (Δ U) values demonstrate greater consistency and lower magnitudes at points 7, 10, 11, and 14 imply fewer vertical shifts or structural modifications in those locations, as illustrated in Fig. 9. Emphasizing regions exhibiting substantial movement can inform maintenance prioritization. Implementing proactive measures for points experiencing ongoing shifts can help prevent future structural problems. The data trends underscore the importance of continuous monitoring, particularly for

points that exhibit significant changes. Routine inspections will uphold the bridge's stability and improve safety standards.

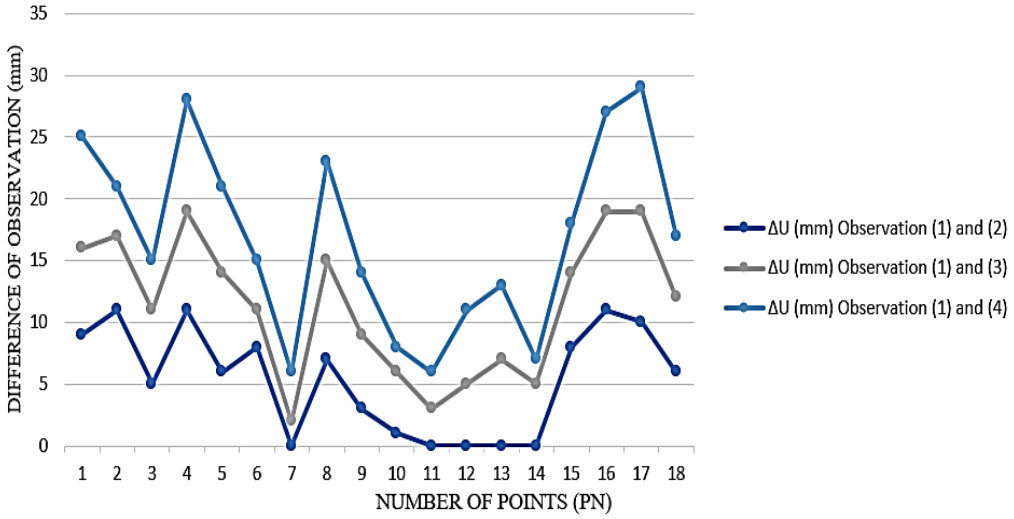


Fig. 9. Changes in Vertical (ΔU) measurements

### 3.2. Thermally Contextualized Inter-Epoch Trends

The analysis involves thermally contextualized trends observed from one session to the next. Four session-mean local ENU datasets (May, July, September, November), combined with the documented ambient temperatures (24/30/27/25 °C; inter-epoch temperature variations ΔT = +6, −3, −2 °C), were utilized to evaluate changes between sessions from May to July, July to September, and September to November at each monitoring location (PN1–PN18). Since the session means were computed from fixed-ambiguity RTK solutions at 1 Hz (see Methods), the inter-epoch differences primarily reflect quasi-static behavior after accounting for short-term ambient vibrations. Subsequently, stations were classified based on whether the primary horizontal component increased during warming (ΔT = +6 °C up to July) and decreased during subsequent cooling (ΔT < 0 thereafter). The classification of inter-epoch trends at each station, in relation to the recorded temperature steps, is summarized in Table 12.

Table 12. Station-wise classification relative to ΔT

| Class (trend with respect to ΔT) | Stations (PN) |
|---|---|
| Anomalous warm step (no apparent increase with +6 °C) | PN7, PN11, PN12, PN13, PN14 |
| Inconsistent with cooling (no relaxation during −3/−2 °C) | PN1, PN2, PN3, PN4, PN5, PN6, PN8, PN9, PN10, PN15, PN16, PN17, PN18 |

This classification improves the understanding of endpoint displacements. Several stations with significant horizontal offsets (such as PN1, PN4, PN5, PN16, PN17) are categorized as "inconsistent with cooling," indicating trends that ΔT alone does not fully explain. These stations are suitable candidates for prioritized engineering analysis. The statistical detectability uses the 95% minimal-detectable shift; changes within the $\pm\tau_{50}$ range are attributed to environmental factors or noise, while exceeding this threshold suggests the presence of detectable structural phenomena.

### 3.3. Results of Geostatistical Analysis

Each measurement station at the Al-Marj City Bridge in Libya conducted geostatistical analysis utilizing the designated IDW method in conjunction with an interpolation tool. Observations one, two, and three for each of the 18 measurement stations were systematically compared through this methodology. A notable finding of this analysis was the comparison between observations (1) and (4), which aimed to identify variations in Easting, Northing, and height over a six-month period. In more detail, the sections highlighted in green show relative stability, with only slight eastward

movement. These green areas indicate that these parts of the bridge have experienced minimal horizontal shifting, suggesting they are less affected by lateral forces like wind or minor seismic events. Moderate deformation levels are observed in the yellow and orange zones. These areas may experience minor displacements attributable to factors such as thermal expansion, slight material settlement, or the incremental accumulation of stress resulting from consistent vehicular traffic. Although these variations are not pronounced, continuous monitoring is essential, as these locations could undergo further shifts under persistent or repeated stress over time.

### *3.3.1 Detailed Analysis of Deformation in the East Direction (ΔE)*

The analysis of deformation in the east direction (ΔE) indicates that the bridge structure undergoes an eastward (horizontal) displacement. A color spectrum, ranging from green to dark red, visually represents the deformation across the structure. Each color corresponds to a specific deformation interval, with green indicating minimal movement and dark red signifying substantial deformation, as depicted in Fig. 10.

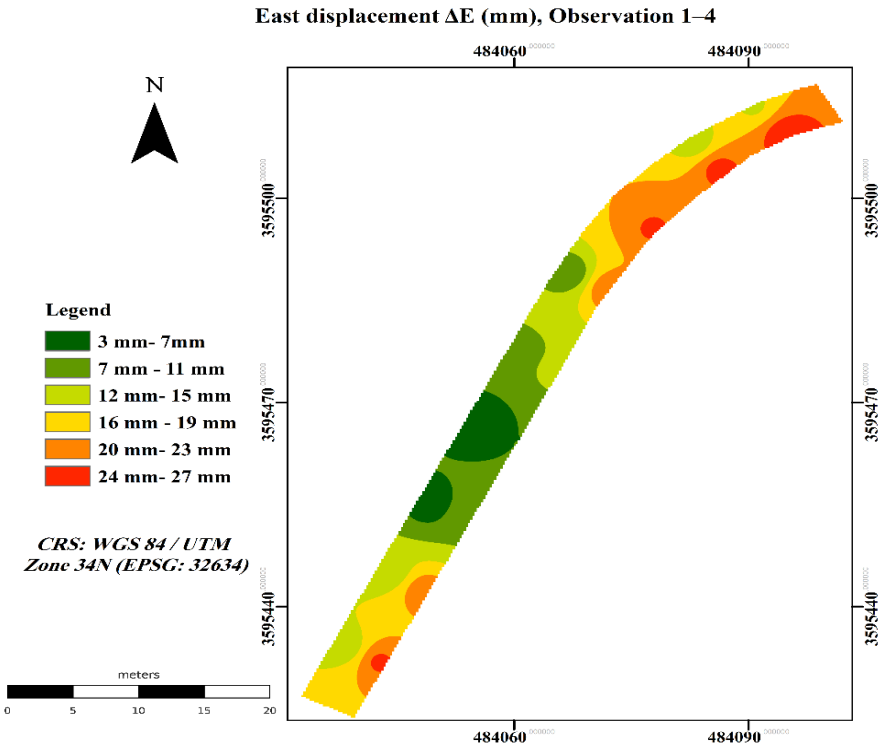


Fig. 10. The geostatistical analysis for Changes in East (Δ E) measurements

The red and dark red regions indicate substantial deformation extending eastward. These areas have experienced considerable horizontal displacement, potentially signifying material stress or strain that could compromise the bridge's structural integrity. Such deformations are likely attributable to external influences, including lateral loads from high winds, uneven ground support, or adjacent construction activities. These zones warrant further examination, as they may represent critical regions subjected to high horizontal stress, which could result in long-term structural deterioration if not properly managed.

The analysis of the east-oriented deformation map offers valuable insights into lateral stability. The prominent red regions potentially signify those particular segments of the bridge are undergoing lateral displacements, which may be attributed to dynamic loads or environmental influences, thereby potentially necessitating reinforcement or adjustments in load distribution.

### *3.3.2 Detailed Analysis of Deformation in the North Direction (ΔN)*

The displacement was measured using a color-coded system, where green indicates stability and red highlights areas with significant movement. Analyzing these longitudinal changes is essential for understanding how stresses affect the bridge and its structural integrity. To identify the sections most impacted by mechanical loads and energy, the bridge was divided into segments based on

different displacement levels. The following discussion outlines each of these regions. Variations in the structure's northern (or longitudinal) direction are shown in Fig. 11.

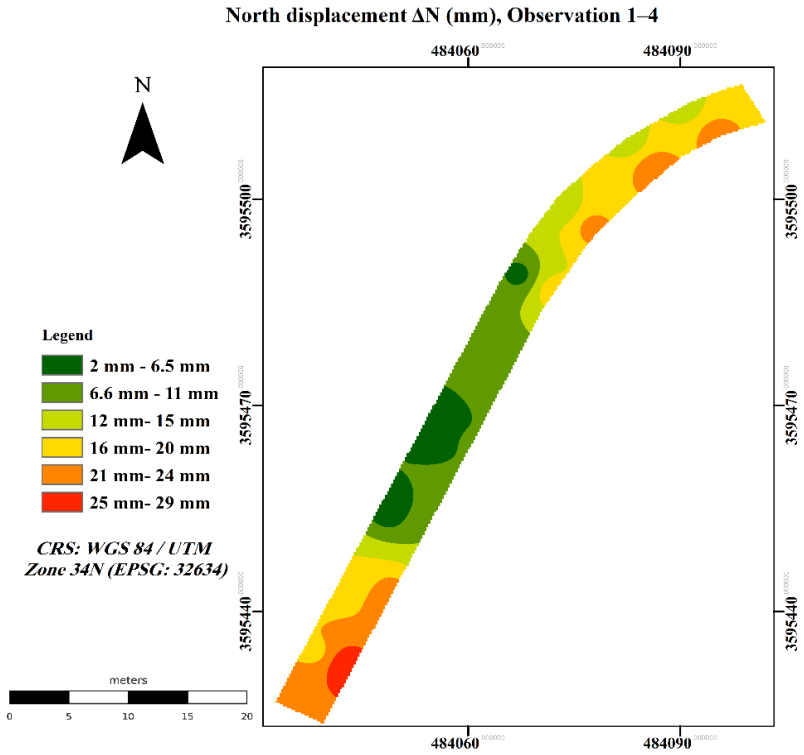


Fig. 11. Geostatistical analysis for Changes in North (Δ N) measurements

The green regions on the northern chart indicate minimal longitudinal displacement. The structural components located within these areas have largely maintained stability against longitudinal forces, such as those originating from vehicle braking, acceleration, or the natural settlement of the bridge. Moderate displacement along the northern axis is observable within the yellow and orange sectors. These variations may be attributed to minor structural settlement or the inherent thermal expansion and contraction of materials. Longitudinal forces, including vehicle loads exerting pressure along the length of the bridge, may also contribute to these moderate shifts. Although currently not a source of concern, continuous monitoring remains essential, as recurrent or increasing load stresses could exacerbate these deformations.

The red zones indicate areas of the bridge exhibiting significant deformation toward the north. Notable longitudinal displacement may suggest material fatigue or issues with the bridge's anchoring system, especially if such displacements are localized. Possible causes include high vehicular traffic, structural creep, or nearby land subsidence. The red regions on the northern-facing map delineate stress concentrations along the bridge, which could compromise the structure's stability if not addressed promptly. Analyzing these deformations in the northward direction is essential for understanding the bridge's response to longitudinal forces. Large displacements along this axis may reveal structural vulnerabilities in managing longitudinal loads, particularly under conditions of heavy traffic or environmental influences.

### *3.3.3 Detailed Analysis of Deformation in Vertical (ΔU)*

Height fluctuations may indicate issues related to structural support or material fatigue, emphasizing the importance of this measurement. Red highlights areas showing significant vertical movement, while green indicates stability. The vertical displacements or height changes of the bridge are shown in Fig. 12. Figure 12 illustrates that the green regions denote the stability of the bridge's vertical position, signifying the absence of vertical displacement or subsidence. This stability is crucial as it affirms that the structure is adequately supported and not susceptible to sinking or rising, which could compromise its integrity. The yellow and orange regions signify moderate vertical displacement, possibly attributable to natural material settling or slight upward movements induced by thermal expansion. Over time, bridges may experience vertical

deformations resulting from factors such as traffic vibrations or minor soil compression. Although these alterations are not substantial, ongoing monitoring remains essential, as their cumulative effects could lead to further settlement.

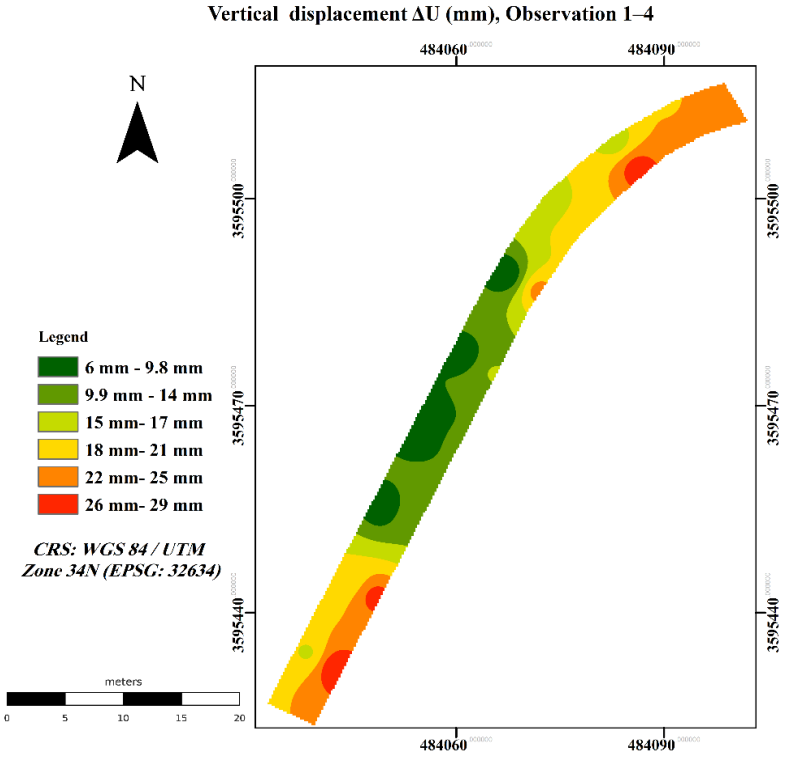


Fig. 12. The geostatistical analysis for changes in Vertical (Δ U) measurements

The dark red areas indicate significant elevation variations, suggesting that certain sections of the bridge may have experienced settlement or considerable uplift. Such phenomena may be attributed to soil subsidence beneath the bridge piers, the impact of recurrent heavy loads, or material deterioration. Vertical deformations generally pose greater risks than horizontal deformations, as they directly threaten the structural integrity of the bridge. Specifically, subsidence may signify foundational instability or complications related to soil compaction and support. The red zones on the elevation map outline locations where structural integrity could be compromised, thus requiring prioritized maintenance or reinforcement. Understanding height variations is crucial for ensuring the bridge's load capacity. Persistent or substantial elevation changes could result in uneven load distribution, thereby increasing stress on specific components. It is essential to address these deformations to prevent potential structural failures.

### 3.4. Cross-Validation Outcomes and Sensitivity to IDW Parameters

The Leave-one-out cross-validation (LOOCV) performed over the parameter grid $p \in \{1, 2, 3\}$ and $k \in \{6, 12\}$ showed a flat error surface, with consistently low prediction errors across all components. The configuration p = 1, k = 6 achieved the lowest (or nearly the lowest) errors for ΔE, ΔN, and ΔU, as shown in Table 12, with RMSE values of 7.25 mm (ΔE), 6.57 mm (ΔN), and 6.78 mm (ΔU). The corresponding MAE values were 6.05 mm, 5.47 mm, and 5.66 mm. These results align with the short-baseline RTK/GNSS repeatability ranges, indicating that discrepancies of about 1–2 mm are within measurement noise. In contrast, spatially consistent shifts of several tens of millimeters are easily noticeable.

The robustness of parameter selection was further confirmed by the consistent stability of hotspot locations and their relative intensities across different (p, k) configurations. The Spearman's ρ rank correlation between the baseline setting (1,6) and other configurations consistently stayed high (around 0.91–0.99 across components). This consistency indicates that the spatial pattern of maxima and minima remains stable under reasonable changes in IDW parameters. Therefore, the (p = 1, k = 6) configuration was chosen for map creation and later analyses.

Table 13. LOOCV error metrics (mm) by IDW parameters.

| Component | p | k | RMSE (mm) | MAE (mm) |
|---|---|---|---|---|
| ΔE | 1 | 6 | 7.25 | 6.05 |
| ΔE | 1 | 12 | 7.42 | 6.45 |
| ΔE | 2 | 6 | 8.04 | 6.95 |
| ΔE | 2 | 12 | 7.97 | 6.86 |
| ΔE | 3 | 6 | 8.87 | 7.84 |
| ΔE | 3 | 12 | 8.83 | 7.80 |
| ΔN | 1 | 6 | 6.57 | 5.47 |
| ΔN | 1 | 12 | 7.05 | 5.67 |
| ΔN | 2 | 6 | 7.05 | 6.46 |
| ΔN | 2 | 12 | 7.04 | 6.34 |
| ΔN | 3 | 6 | 7.76 | 7.30 |
| ΔN | 3 | 12 | 7.72 | 7.26 |
| ΔU | 1 | 6 | 6.78 | 5.66 |
| ΔU | 1 | 12 | 7.05 | 5.82 |
| ΔU | 2 | 6 | 7.54 | 6.57 |
| ΔU | 2 | 12 | 7.45 | 6.43 |
| ΔU | 3 | 6 | 8.35 | 7.42 |
| ΔU | 3 | 12 | 8.29 | 7.37 |

*Note: Coordinates used for calculating planar distances were obtained from the initial-epoch UTM positions. Conversely, the target validation values included displacements at the endpoints (from point 1 to point 4), measured in millimeters.*

### 3.5. Station-Level Detectability Screening ($\tau_{95}$& Persistence)

Using the 95% thresholds defined in Methods (horizontal $\tau_{95,h}$ = 6 mm; vertical $\tau_{95,v}$ = 12 mm) with a persistence criterion (exceedance in both 1→3 and 1→4), the following stations are statistically detectable and thus structurally relevant:

- Multi-component (ΔE, ΔN, ΔU): PN1, PN2, PN4, PN5, PN8, PN15, PN16, PN17 (each exceeds the relevant $\tau_{95}$ and persists across epochs).
- Horizontal only: PN6 and PN18 (ΔE and ΔN exceed $\tau_{95,h}$; ΔU remains ≤ $\tau_{95,v}$).
- Single-component local signals: PN3 (ΔN only) and PN9 (ΔE only).

Stations PN7, PN10–PN14 consistently demonstrate noise levels within acceptable limits and are distinguished by non-persistent fluctuations. These station-specific classifications align with the LOOCV results, thereby affirming the reliability of the identified hotspots regardless of the IDW parameters. Consequently, they are suitable for prioritizing inspections, including joints and bearings at PN1, PN4, and PN5, as well as abutment transitions at PN16–PN17.

### 3.6. Structural Interpretation of The High-Displacement Stations

The most significant and persistent offsets are concentrated at interfaces where restrictions or support compliance may influence observed patterns. PN1, PN4, and PN5 are situated near expansion joints and their supporting bearings; the combined increase in ΔE–ΔN, together with variability in ΔU, indicates deterioration of joint seals, accumulation of debris, contamination, or misalignment of bearings. These conditions restrict thermal or live-load movements and provoke secondary vertical actions. Conversely, PN16 and PN17 are positioned near the transition between the approach slab and the abutment, where more conspicuous ΔU and directional shifts in ΔE/ΔN suggest differential settlement or void formation, as well as a loss of slab support at the backwall interface. These location-specific mechanisms align with the detectability screening (utilizing 95% thresholds) and the LOOCV-robust hotspot patterns, which necessitate targeted verification procedures. Such procedures include inspecting joint gaps and seals, removing debris at PN1/PN4/PN5, assessing for lift-off and rotation, and conducting visual inspections of bearings at these points. Furthermore, sounding or void detection, alongside re-support or lifting of the slab at

PN16/PN17, is recommended. Re-measuring after remedial actions can help confirm the normalization of movements.

### 3.7. RTK-GNSS Bridge Deck Displacements: Significance, Codes, and Maintenance Priorities

Inter-epoch translations predominantly occur at the millimeter scale and should be assessed in conjunction with the practical resolution limits of short-baseline RTK/GNSS systems. Recent stability assessments conducted in open environments indicate standard deviations of approximately ≤~8 mm, suggesting that variations of 1–2 mm are near the noise floor inherent to monitoring systems. Such variations do not inherently imply adverse structural behavior when evaluated in isolation. Conversely, localized spatial shifts of approximately 25–30 mm across the monitoring area suggests detectable and coherent movements, which warrant engineering review and further investigation [40]. In summary, minor discrepancies are generally attributed to the noise measurement, whereas larger, spatially organized deviations may indicate potential serviceability issues.

These observations should be incorporated into the relevant regulatory framework. Major bridge standards do not specify fixed millimeter thresholds for deck survey points; instead, serviceability is assessed at the member or system level using span deflection criteria rather than absolute deck displacements. According to AASHTO LRFD, live-load deflection limits range from L/800 to L/1000, with more restrictive limits for pedestrian comfort. GNSS-derived ENU translations in this study mainly serve for trend analysis and prioritizing inspections and maintenance, while compliance with code requirements is independently verified through member-level assessments [41-42]. These measurements act as a screening tool, while code evaluations determine structural acceptability.

Translating these findings into actionable steps, mapped zones exhibiting consistent peaks in ΔE/ΔN/ΔU and demonstrating upward trends over successive periods serve as dependable early indicators of emerging issues. These “problematic zones” should be prioritized for targeted field verification and, upon verification, for the implementation of preventive measures. Key locations often include expansion joints (seal damage, debris, bond loss), bearings (contamination, misalignment, limited movement), approach-slab–abutment transitions (differential settlement, voiding), and deck drainage pathways (clogged scuppers, compromised waterproofing). A clear workflow is recommended: first, verify each hotspot through close-range visual inspection or MMS evaluation; second, execute necessary repairs such as joint resealing, bearing cleaning or resetting, slab lifting or void filling, and drainage clearing with waterproofing restoration; third, re-measure to confirm resolution of the issue. For planning purposes, hotspots identified by the detectability criterion that persist across two or more consecutive periods should be accorded with higher priority in maintenance activities and should continue to be monitored until stability is confirmed.

## 4. Conclusions

A reproducible multi-epoch real-time kinematic workflow was established under strict quality assurance, converting GNSS observations into component-level displacement vectors (ΔE, ΔN, ΔU) within a fixed local East, North, Up reference frame and synthesizing them into decision-oriented indicators via a deck-masked GIS layer. Four traffic-free epochs (May to November 2024) across 18 stations were referenced to a stable local datum at R1 and independently verified at R2 through dual-frequency static sessions with minimally constrained adjustment. Field acquisitions employed fixed-ambiguity solutions (15° elevation mask, PDOP ≤ 4), resulting in fix ratios of 99.0–99.3%, a median PDOP of 1.66–1.83, and a median satellite count of 12–14; practical repeatability was approximately 4–6 mm horizontally and 7–12 mm vertically.

To distinguish quasi-static deformation from inherent dynamic responses, each station was monitored for approximately 15 minutes at a frequency of 1 Hz under calm, dry conditions with deck closures enforced. Data series were accepted only when they exhibited fixed integers and were subsequently averaged following quality control procedures, which serve to diminish high-frequency content associated with wind- or traffic-induced vibrations and diurnal micro-

oscillations. Ambient conditions were recorded for each epoch, including temperature and wind conditions, in conjunction with displacement summaries. Measurements were intentionally scheduled outside peak thermal transient periods and active traffic intervals. Collectively, the implementation of (i) traffic suppression, (ii) meteorological screening, and (iii) fixed-solution averaging provides a justifiable foundation for interpreting the reported displacements as quasi-static during the campaign periods.

No controlled load testing was conducted in this study; the objective was to characterize repeatable, quasi-static components under standard environmental conditions with traffic absent during all occupation periods. Therefore, the reported endpoint contrasts represent traffic-free, meteorologically screened states rather than forced-vibration responses. Displacements at the campaign-to-baseline endpoint (comparing 3 May and 4 November 2024) were measured in millimeters: ΔE reached a maximum of 27 mm at PN1, ΔN reached 29 mm at PN17, and ΔU also reached 29 mm at PN17. Five stations, PN1, PN4, PN5, PN16, and PN17, exceeded 20 mm in two or more components, thereby defining priority locations for follow-up inspection. A deck-constrained GIS representation provided spatial coherence to the station-wise signals, generating auditable map products with explicit millimeter units and revealing deck-scale gradients that were not evident in tables alone.

The contribution introduces a data-to-decision pipeline that stabilizes a local ENU realization through repeatable, quality-controlled RTK solutions. It integrates the resultant vectors with GIS-based analytics to produce traceable, condition-relevant indicators rather than merely plot-only summaries. Limitations of this approach include the absence of controlled load tests and the lack of direct benchmarking against PPP/PPP-AR/PPP-RTK or external services such as CSRS-PPP. Future efforts will involve staged loading with wind and temperature covariates, direct RTK–PPP comparisons on the same testbed, and improved threshold-based GIS alerting focusing on PN1, PN4, PN5, PN16, and PN17.

## Acknowledgement

This research was made possible by financial support from University Tun Hussein Onn Malaysia and the UTHM Publisher's Office through the Publication Fund E15216.

## References

[1] Xiong C, Wang M, Chen W. Data analysis and dynamic characteristic investigation of large-scale civil structures monitored by RTK-GNSS based on a hybrid filtering algorithm. J Civ Struct Health Monit. 2022;12(4):857–874. https://doi.org/10.1007/s13349-022-00580-6

[2] Xi R, He Q, Meng X. Bridge monitoring using multi-GNSS observations with high cutoff elevations: A case study. Measurement. 2021;168:108303. https://doi.org/10.1016/j.measurement.2020.108303

[3] Zhao L, et al. A novel low-cost GNSS solution for the real-time deformation monitoring of cable saddle pushing: A case study of Guojiatuo suspension bridge. Remote Sens (Basel). 2022;14(20):5174. https://doi.org/10.3390/rs14205174

[4] Xi R, et al. Performance assessment of structural monitoring of a dedicated high-speed railway bridge using a moving-base RTK-GNSS method. Remote Sens (Basel). 2023;15(12):3132. https://doi.org/10.3390/rs15123132

[5] Ju B, et al. Performance evaluation of GNSS kinematic PPP and PPP-IAR in structural health monitoring of bridge: Case studies. Measurement. 2022;203:112011. https://doi.org/10.1016/j.measurement.2022.112011

[6] Soldatkin M, et al. Experimental research of a structural health monitoring system concept based on fiber Bragg grating sensors on composite panels of an aircraft. Research on Engineering Structures and Materials. 2024. https://doi.org/10.17515/resm2024.287cs0514rs

[7] Hu X, et al. High-resolution, high-speed and low-cost flexible tactile sensor array system. Measurement. 2025;241:115630. https://doi.org/10.1016/j.measurement.2024.115630

[8] Bhavana P, et al. Integrating self-sensing nano composite and fiber optic sensors technologies for advancing structural monitoring: A mini review. Research on Engineering Structures and Materials. 2024. https://doi.org/10.17515/resm2024.362ma0722rv

[9] Schiettekatte LR, Garrido MS, de Lacy MC. Use of GNSS and ERA5 precipitable water vapor based standardized precipitation conversion index for drought monitoring in the Mediterranean coast: A first

case study in Southern Spain. Adv Space Res. 2023;72(9):3946–3959. https://doi.org/10.1016/j.asr.2023.08.030
[10] de Blas FJ, et al. The Galileo high accuracy service (HAS): A pioneer free-of-charge global precise positioning service. In: Proceedings of the 36th International Technical Meeting of the Satellite Division of The Institute of Navigation (ION GNSS+ 2023). 2023. p. 449–468. https://doi.org/10.33012/2023.19197
[11] Zhang X, et al. Performance of PPP and PPP-RTK with new-generation GNSS constellations and signals. Satell Navig. 2025;6(1):17. https://doi.org/10.1186/s43020-025-00169-6
[12] Li X, et al. Review of PPP–RTK: Achievements, challenges, and opportunities. Satell Navig. 2022;3(1):28. https://doi.org/10.1186/s43020-022-00089-9
[13] Motella B, Margaria D, Paonni M. SNAP: An authentication concept for the Galileo open service. In: 2018 IEEE/ION Position, Location and Navigation Symposium (PLANS). IEEE; 2018. p. 967-977. https://doi.org/10.1109/PLANS.2018.8373475
[14] Dymkova S. Earth observation and global navigation satellite systems analitical report part I (aviation and space). Synchroinfo J. 2022;8(1):30-41. https://doi.org/10.36724/2664-066x-2022-8-1-30-41
[15] Franciosi M, Kasser M, Viviani M. Digital twins in bridge engineering for streamlined maintenance and enhanced sustainability. Autom Constr. 2024;168:105834. https://doi.org/10.1016/j.autcon.2024.105834
[16] Gao Y, Xiong G, Hu Z, Chai C, Li H. Bridge digital twin for practical bridge operation and maintenance by integrating GIS and BIM. Buildings. 2024;14(12). https://doi.org/10.3390/buildings14123731
[17] Xie Y, Meng X, Nguyen DT, Xiang Z, Ye G, Hu L. A discussion of building a smart SHM platform for long-span bridge monitoring. Sensors. 2024;24(10):3163. https://doi.org/10.3390/s24103163
[18] Paziewski J, Wielgosz P. Investigation of some selected strategies for multi-GNSS instantaneous RTK positioning. Adv Space Res. 2017;59(1):12–23.
[19] Rădulescu VM, Rădulescu GMT, Naș SM, Rădulescu AT, Rădulescu CM. Structural Health Monitoring of Bridges under the Influence of Natural Environmental Factors and Geomatic Technologies: A Literature Review and Bibliometric Analysis. Buildings. 2024;14(9):2811. https://doi.org/10.3390/buildings14092811
[20] Buka-Vaivade K, Nicoletti V, Gara F. Advancing bridge resilience: a review of monitoring technologies for flood-prone infrastructure. Open Res Europe. 2025;5:26. https://doi.org/10.12688/openreseurope.19232.2
[21] An X, Meng X, Hu L, Xie Y, Zhang F, Pan S. GNSS integrated displacement and attitude determination for structural health monitoring of long-span bridges. Satell Navig. 2025;6(1):19. https://doi.org/10.1186/s43020-025-00174-9
[22] Sotoudeh S, Lantini L, Uzor S, Tosti F. A Systematic Review into the Application of Ground-Based Interferometric Radar Systems for Bridge Monitoring. Remote Sens (Basel). 2025;17(9):1541. https://doi.org/10.3390/rs17091541
[23] Lantsoght EOL. Assessment of existing concrete bridges by load testing: barriers to code implementation and proposed solutions. Struct Infrastructure Eng. 2024;20(7–8):1002–1014. https://doi.org/10.1080/15732479.2023.2264825
[24] Zhang B, Ren Y, He S, Gao Z, Li B, Song J. A review of methods and applications in structural health monitoring (SHM) for bridges. Measurement. 2024:116575. https://doi.org/10.1016/j.measurement.2024.116575
[25] Qu X, Ding X, Li X, Yu W, Xu YL. Assessing and Mitigating impacts of structural inclination on acceleration measurements and estimated displacements using integrated GNSS and accelerometer structural health monitoring systems. Measurement. 2025;253:117578. https://doi.org/10.1016/j.measurement.2025.117578
[26] Robustelli U, Cutugno M, Pugliano G. Low-Cost GNSS and PPP-RTK: Investigating the Capabilities of the u-blox ZED-F9P Module. Sensors. 2023;23(13):6074. https://doi.org/10.3390/s23136074
[27] Chen M, Zhao L, Zhai W, Lv Y, Jin S. Assessment of the real-time and rapid precise point positioning performance using geodetic and low-cost GNSS receivers. Remote Sens (Basel). 2024;16(8):1434. https://doi.org/10.3390/rs16081434
[28] Oku Topal G, et al. Performance of low-cost GNSS in structural health monitoring studies: shake table tests. Exp Tech. 2024;48(6):977–989. https://doi.org/10.1007/s40799-024-00710-3
[29] Zenk D, Gillins D. Classifications, standards, and specifications for GNSS geodetic control surveys using OPUS Projects. 2024.
[30] Vázquez-Ontiveros JR, et al. Implementation of PPP-GNSS measurement technology in the probabilistic SHM of bridge structures. Measurement. 2020:108677. https://doi.org/10.1016/j.measurement.2020.108677

[31] Hou C, Shi J, Ouyang C, Guo J, Zou J. A dual-base station constraint method to improve deformation monitoring precision consistency in strip regions. Satell Navig. 2024;5(1):26. https://doi.org/10.1186/s43020-024-00148-3
[32] Xie Y, Zhang S, Meng X, Nguyen DT, Ye G, Li H. An innovative sensor integrated with GNSS and accelerometer for bridge health monitoring. Remote Sens (Basel). 2024;16(4):607. https://doi.org/10.3390/rs16040607
[33] Armijo A, Zamora-Sánchez D. Integration of railway bridge structural health monitoring into the internet of things with a digital twin: a case study. Sensors. 2024;24(7):2115. https://doi.org/10.3390/s24072115
[34] Achite M, Tsangaratos P, Pellicone G, Mohammadi B, Caloiero T. Application of multiple spatial interpolation approaches to annual rainfall data in the Wadi Cheliff basin (north Algeria). Ain Shams Eng J. 2024;15(3):102578.
[35] Figueiredo E, Brownjohn J. Three decades of statistical pattern recognition paradigm for SHM of bridges. Struct Health Monit. 2022;21(6):3018–3054. https://doi.org/10.1016/j.asej.2023.102578
[36] Ismail S, Ahmed MF. GIS-based spatio-temporal and geostatistical analysis of groundwater parameters of Lahore region Pakistan and their source characterization. Environ Earth Sci. 2021;80(21):719. https://doi.org/10.1007/s12665-021-10034-9
[37] Masoudi M. Estimation of the spatial climate comfort distribution using tourism climate index (TCI) and inverse distance weighting (IDW)(case study: Fars Province, Iran). Arab J Geosci. 2021;14(5):363. https://doi.org/10.1007/s12517-021-06605-6
[38] Sadeghi B, Eleish AM, Morrison SM, Klump J. Inverse radius weighting and its python package 'IRWPy': A new topography-informed interpolation to enhance geological interpretations. Ore Geol Rev. 2024;172:106206. https://doi.org/10.1016/j.oregeorev.2024.106206
[39] Barudžija U, Ivšinović J, Malvić T. Selection of the value of the power distance exponent for mapping with the inverse distance weighting method—application in subsurface porosity mapping, Northern Croatia Neogene. Geosciences (Basel). 2024;14(6):155. https://doi.org/10.3390/geosciences14060155
[40] Yasin KH, Gelete TB, Iguala AD, Kebede E. Optimal interpolation approach for groundwater depth estimation. MethodsX. 2024;13:102916. https://doi.org/10.1016/j.mex.2024.102916
[41] Fleit G. Windowed anisotropic local inverse distance-weighted (WALID) interpolation method for riverbed mapping. Acta Geophys. 2025;73(3):2819–2833. https://doi.org/10.1007/s11600-024-01510-4
[42] Qi W, Li F, Yu L, Fan L, Zhang K. Analysis of GNSS-RTK Monitoring Background Noise Characteristics Based on Stability Tests. Sensors. 2025;25(2):379. https://doi.org/10.3390/s25020379
[43] Bartz JR, Blatz JA. Comparison of Canadian Highway Bridge Design Code and AASHTO LRFD Bridge Design Specifications regarding pile design subject to negative skin friction. Can Geotech J. 2020. https://doi.org/10.1139/cgj-2019-0247